atmosphere

MDPI

Article

A Reduced-Order Regime Theory for Aerosol–Halogen–Dynamics Coupling in Volcanic Super-Eruptions

Sebastiano Ettore Spoto

Dipartimento di Scienze della Terra, Università degli Studi di Firenze, 50121 Florence, Italy; sebastianoettore.spoto@unifi.it

Abstract

Volcanic super-eruptions can perturb atmospheric composition and climate-relevant radiative properties in ways that are not captured by simple scaling from Pinatubo-like events. This study presents a reduced-order regime theory for the coupled evolution of stratospheric sulfur, sulfate aerosol burden, reactive halogens, ozone loss, stratospheric thermal adjustment, and aerosol residence time. The analysis is intended as an interpretive tool for organizing sulfur-rich volcanic scenarios, comparing literature-based benchmark classes, and designing chemistry–climate model experiments, rather than as an event-specific calibration or a substitute for three-dimensional models. Four control parameters structure the response: sulfur loading relative to microphysical saturation, effective halogen strength, ash-uptake efficiency, and dynamical lifetime sensitivity, with hemispheric asymmetry treated diagnostically. An external consistency check against published Pinatubo-like, idealized 10–40 teragrams of sulfur (Tg S), Toba-like, and Los Chocoyos-like responses is used to evaluate whether the reduced theory reproduces the expected rank ordering of aerosol saturation, forcing-efficiency decline, ozone-loss amplification, ash-driven sulfur suppression, and residence-time sensitivity. This comparison does not assign pointwise error margins against three-dimensional model output; it evaluates regime membership, sign of response, rank ordering, and broad magnitude behavior. The main conclusion is that volcanic super-eruption impacts are governed by interacting regime transitions rather than by sulfur mass alone. Microphysical saturation can limit forcing efficiency, halogens can shift the system toward chemically amplified ozone depletion, ash uptake can reduce the effective sulfur burden during the early phase, and dynamical state can control persistence and hemispheric expression. By separating these mechanisms, the study provides a compact basis for interpreting large volcanic perturbations to atmospheric chemistry and for designing targeted model experiments on extreme eruption scenarios.

Keywords: volcanic super-eruptions; stratospheric sulfate aerosol; volcanic halogens; ozone depletion; stratospheric dynamics; reduced-order analysis; regime theory

Academic Editor: Avelino Eduardo Saez

Received: 23 April 2026
Revised: 10 June 2026
Accepted: 11 June 2026
Published: 13 June 2026

1. Introduction

This study concerns volcanic sulfur-rich super-eruptions; non-volcanic sulfur releases or other sulfur-containing industrial or extraterrestrial emission scenarios are outside its scope. Large explosive volcanic eruptions influence the atmosphere through the stratospheric injection of sulfur-bearing gases that oxidize to sulfate aerosol and, when halogens are co-injected, through chemically active chlorine- and bromine-driven perturbations to ozone. They therefore modify shortwave reflection, longwave absorption, heterogeneous chemistry, stratospheric temperatures, circulation, and ultimately surface climate [1–3].

https://doi.org/10.3390/atmos17060606

The canonical Pinatubo paradigm remains indispensable, but it does not exhaust the physics of much larger eruptions because the relation among injected sulfur mass, particle size, aerosol optical depth, and residence time is not linear once coagulation and sedimentation begin to reorganize the plume microphysics [4–8]. Volcanic forcing efficiency is furthermore sensitive to source latitude, injection height, eruption season, and model physics, with meaningful variability already evident for events within or near the historical range [9–12].

The super-eruption problem is therefore not merely a question of amplitude. At sufficiently large sulfur loadings, larger particles are generated, residence times may shorten, and the additional radiative forcing obtained per unit sulfur can decline rather than remain constant [4,5,7,8]. Recent large-ensemble calculations indicate an approximately linear climate response over an idealized tropical range of roughly 10–40 teragrams of sulfur (Tg S), but this result does not imply linearity at super-eruption scale; rather, it highlights a finite window beyond which saturation should be expected [7]. The saturation issue is not merely radiative. Aerosol size affects sedimentation, tropical self-lofting, heterogeneous chemistry, and hemispheric transport, thereby coupling microphysics directly to chemistry and dynamics [2,5,6,13].

A second nonlinearity arises from volcanic halogens. A growing literature demonstrates that sulfur-rich eruptions co-emitting reactive chlorine and bromine can induce large or even extreme ozone losses, substantially enhance surface ultraviolet (UV) radiation, and modify the aerosol evolution indirectly by changing the stratospheric thermal structure [14–18]. The co-emission of sulfur and halogens has been shown to amplify effective radiative forcing (ERF) because ozone depletion cools the stratosphere, reduces aerosol self-lofting, and thereby changes the spatiotemporal structure of the aerosol cloud [16]. Such behavior cannot be captured by sulfur-only scaling arguments.

A third nonlinearity arises from ash. Persisting ash has been shown to accelerate sulfur removal by heterogeneous uptake of sulfur dioxide (SO_2), thereby reducing the amount of sulfur available for sulfate aerosol formation and altering aerosol optical properties [19]. Because ash acts early, before aerosol growth has fully unfolded, it can displace the system across multiple thresholds simultaneously: the sulfate burden threshold for forcing saturation, the surface-area threshold for ozone loss, and the heating threshold for self-lofting. Ash therefore belongs in any general super-eruption theory even if its residence time is much shorter than the sulfate lifetime [19].

A fourth nonlinearity arises from atmospheric dynamics. The volcanic response of the stratosphere and troposphere depends not only on radiative forcing magnitude but also on the pre-existing circulation state, the season of eruption, the latitude of injection, and the internal variability of the middle atmosphere [9,20–22]. Aerosol-induced stratospheric warming can shift jets poleward through a combination of zonal-mean thermal wind adjustment and eddy feedback [20]. The quasi-biennial oscillation (QBO) can be perturbed by historical eruptions and, in modeled super-eruption cases, may be disrupted for several years to a decade [23,24]. Even with fixed source parameters, initial atmospheric conditions can substantially alter sulfur transport, hemispheric asymmetry, aerosol effective radius, radiative forcing, and ozone impacts [22].

The paleoclimate literature reinforces the need for a reduced-order interpretation rather than a single-event narrative. Modeling studies of Toba and Los Chocoyos have explored severe ozone depletion, regional climate heterogeneity, and decadal stratospheric dynamical disruption, whereas recent ice-core evidence for Los Chocoyos disputes a millennial-scale climate effect [15,18,25,26]. These results collectively suggest that extreme short-lived atmospheric perturbation need not map onto proportionally extreme long-duration cooling, and they motivate a theory that is explicit about which aspects of the response are controlled by sulfur loading, chemical coupling, and atmospheric state.

The purpose of the present manuscript is to develop a reduced-order analysis of aerosol–halogen–dynamics coupling under super-eruption conditions. The analysis couples sulfur conversion, aerosol growth, ash scavenging, halogen-driven ozone loss, radiative adjustment, and state-dependent residence time within a mathematically transparent regime model. The intention is not to replace three-dimensional chemistry–climate simulations or existing volcanic forcing emulators but to provide an analytical tool for interpreting existing results, designing idealized experiment suites, and benchmarking model hierarchies [3,12,22,27]. The central thesis is that super-eruption response is structured by thresholds: a sulfur-loading threshold marks the onset of microphysical saturation, a halogen-surface-area threshold marks chemically amplified ozone depletion, an ash-uptake threshold reduces sulfur yield into sulfate, and a thermodynamic threshold determines whether aerosol heating or ozone-loss cooling dominates the bulk stratospheric adjustment.

The contribution of the present analysis is fourfold. First, a single reduced-order closure is written for sulfur, sulfate aerosol burden, reactive halogens, ozone loss, and stratospheric thermal anomaly. Second, transparent control parameters are isolated in the form of $(\Pi_S, \Pi_H, Da_A, \chi)$, while hemispheric asymmetry is treated diagnostically through a separate coordinate ψ. Third, asymptotic scaling laws are derived for optical depth, surface area, sedimentation, and forcing efficiency. Fourth, the dimensionless control space is benchmarked against representative eruption classes through explicit order-of-magnitude mappings, worked input ranges, and uncertainty sectors. The resulting model is intended as a reduced-order interpretive tool rather than as a calibrated predictive surrogate. To keep the scope explicit, Section 7 distinguishes results shown directly by the reduced theory from broader hypotheses that it suggests for chemistry–climate interpretation and model-hierarchy design.

The analysis is organized around five research propositions. *P1*: microphysical saturation causes forcing efficiency to decline once particle-number growth becomes sublinear. *P2*: halogen-driven ozone loss becomes order-one when the halogen–surface-area product crosses a chemical threshold. *P3*: early ash uptake shifts both radiative and chemical thresholds by suppressing the effective sulfur yield entering the sulfate reservoir. *P4*: lifetime response depends on the sign of the reduced thermal anomaly and on the dynamical confinement state. *P5*: benchmark sectors in reduced control space can organize published Pinatubo-like, transition-corridor, Toba-like, and Los Chocoyos-like results as interpretive regime placements without requiring event-calibrated inversion.

2. Materials and Methods: Empirical and Modeling Basis for a Nonlinear Theory

2.1. Sulfate Aerosol Forcing Is Not Indefinitely Scalable

The sulfate aerosol literature already contains the essential ingredients of a saturation theory. Reviews of the stratospheric aerosol layer emphasize that optical properties, sedimentation, and chemical reactivity depend jointly on burden and size, not on mass alone [2]. The microphysical simulations of Pinatubo and Toba demonstrated that very large sulfur injections generate larger particles that sediment more rapidly, weakening the climatic effect relative to naive linear expectations [4]. Radiative-heating studies further showed that aerosol self-lofting can alter transport pathways and residence times but that this process depends on particle size and the vertical temperature response [5]. Subsequent model intercomparisons and sensitivity studies have confirmed that source height, source magnitude, and model microphysics materially influence the forcing realized for a given sulfur injection [6,10–12].

Two recent developments sharpen the problem. First, a large-ensemble study found that global and hemispheric near-surface temperature and precipitation anomalies can be approximately linearly scalable for idealized tropical eruptions over a moderate sulfur-emission range of about 10–40 Tg S [7]. Second, a dedicated analysis of very large eruptions found saturation in both forcing efficiency and temperature response, with no model simulations producing arbitrarily large effective radiative forcing [8]. These results are not contradictory. They imply that a finite linear window exists but that a transition into a super-eruption regime must occur once burden-dependent particle growth and removal dominate the response. An explicit threshold formalism is therefore justified.

2.2. Halogen-Rich Eruptions Define a Distinct Chemical Regime

A sulfur-only treatment is incomplete because explosive eruptions may also inject large quantities of chlorine and bromine into the stratosphere, as inferred from petrological volatile budgets and stratospheric halogen-delivery studies [14,15,17,28–31]. Modeling studies have demonstrated that pre-industrial tropical eruptions can cause substantial global ozone depletion and large ultraviolet enhancement [14]. For a sulfur- and halogen-rich Los Chocoyos analog, elevated aerosol loading, long-lived halogen perturbation, pronounced ozone destruction, and strong UV increase were simulated [15]. A Toba-like sulfur-rich event has likewise been argued to be capable of severe tropical stratospheric ozone depletion [18].

The decisive conceptual point is that halogens do not act independently of aerosol microphysics. Heterogeneous activation proceeds on aerosol surface area, which itself depends on burden and effective radius [2,16]. The co-emission of sulfur and halogens has been shown to amplify volcanic effective radiative forcing by altering stratospheric ozone and, through ozone-induced cooling, suppressing aerosol self-lofting and thereby reshaping aerosol evolution [16]. Sensitivity to latitude, season, and halogen content has also been demonstrated for contemporary explosive-eruption scenarios [17]. The sulfur budget and the ozone budget must therefore be solved as a coupled problem.

2.3. Ash Modifies Sulfur Availability Before the Sulfate Cloud Fully Forms

Ash is often treated as a transient by-product, yet recent work demonstrated that persisting ash can substantially reduce stratospheric SO_2 lifetime and modify the aerosol optical properties by promoting sulfur uptake onto ash surfaces [19]. The timing of this process is crucial. Sulfur scavenging by ash acts during the early plume stage, before the sulfate burden, effective radius, and aerosol surface area have reached their mature values. The process therefore modifies not only total sulfate mass but also which microphysical regime the plume can access. A theory that ignores ash may overestimate both radiative forcing and ozone loss in ash-rich cases, particularly when sulfur emission is close to the onset threshold for microphysical saturation [19].

2.4. Dynamical Adjustment Is State-Dependent

The dynamical response to volcanic forcing is not solely a function of aerosol burden. Stratospheric heating can shift the jets poleward and induce tropospheric changes through a combination of thermal-wind adjustment and eddy interaction [20]. The middle atmosphere is itself highly variable, with the QBO, Brewer–Dobson circulation, and planetary-wave forcing modulating tropical confinement and extratropical export [21]. Historical eruption simulations show that the QBO response depends on its initial phase, while super-eruption simulations suggest that a decadal-scale disruption is possible [23,24].

The strongest recent evidence for explicit state dependence comes from ensemble calculations showing that identical eruption source parameters can still produce substantial differences in sulfur transport, hemispheric stratospheric aerosol optical depth (SAOD) asymmetry, effective radius, forcing, and ozone response due solely to different initial atmospheric conditions [22]. This result implies that a super-eruption theory must include at least one parameter representing the internal dynamical state. It is not necessary that such a parameter resolve every dynamical degree of freedom. It is sufficient that the parameter encode, in reduced form, the aspects of the circulation most relevant to confinement, meridional export, and asymmetry.

2.5. The Unresolved Theoretical Problem

The literature therefore supplies the empirical and numerical ingredients for a regime theory, but not yet a single compact regime-oriented formulation that integrates sulfur loading, halogen activation, ash uptake, and dynamical-state sensitivity in a common control space. Sulfur loading matters, but not linearly [4,7,8]. Halogens matter, but through aerosol surface area and temperature-mediated feedbacks [15,16]. Ash matters early and nonlinearly [19]. Dynamics matter in a state-dependent way [20,22]. What remains less developed is an integrated reduced-order regime analysis that places these processes into a common mathematical structure and yields transparent control parameters, thresholds, and asymptotic scalings. The following sections address that more specific gap.

3. Materials and Methods: Reduced-Order Formulation

3.1. State Variables and Conceptual Architecture

The conceptual structure of the reduced-order theory is shown in Figure 1. The stratospheric system is represented by the state variables

$$S(t), \qquad B(t), \qquad N_c(t), \qquad H(t), \qquad X(t), \qquad T_s(t),$$

The state variables are carried on a sulfur-equivalent basis unless stated otherwise. Here S denotes the sulfur-equivalent gas-phase burden residing in the stratospheric sulfur dioxide (SO_2) reservoir, B denotes the sulfur-equivalent sulfur burden already incorporated into sulfate aerosol, N_c denotes aerosol particle number column, H denotes an effective reactive-halogen burden, X denotes fractional ozone loss relative to a background column Ω_b, and T_s denotes a representative stratospheric thermal anomaly. Whenever aerosol density or particle geometry is required, the corresponding dry sulfate-aerosol mass is written as $B_{\mathrm{aer}} = \nu_{\mathrm{sulf}} B$, where ν_{sulf} is a fixed conversion factor. A single signed dynamical parameter χ is introduced to represent, in compressed form, the combined influence of eruption season, injection latitude, QBO state, and residual-circulation structure on bulk residence time [9,22,23]. Hemispheric asymmetry is represented separately by a diagnostic coordinate ψ so that the model does not impose a one-to-one relation between residence time and hemispheric partitioning. Throughout the manuscript, the sign convention is chosen such that positive χ denotes comparatively confined states, whereas negative χ denotes more export-prone states. For any concrete eruption context, the preferred hemisphere denotes the hemisphere toward which the initial circulation state biases early net export, whereas the opposite hemisphere denotes the complementary branch. For example, in a tropical benchmark case whose early aerosol export is biased northward by the initial circulation, the Northern Hemisphere is the preferred hemisphere and the Southern Hemisphere is the opposite branch; if the early export bias is reversed, the labels reverse as well.

The effective halogen coordinate H should be interpreted as a reduced activity variable rather than as a prognostic chemical species. It aggregates the ability of chlorine- and bromine-bearing volcanic emissions to drive catalytic ozone loss after stratospheric delivery and conversion into reactive forms. This aggregation is appropriate for threshold and regime analysis, but it is not intended to predict quantitative chlorine–bromine partitioning, odd-nitrogen coupling, or full ozone-column recovery; those quantities require a resolved chemistry–climate model.

Table 1 gives the condensed notation used in the main text; the expanded symbol table is retained in Appendix E for reference.

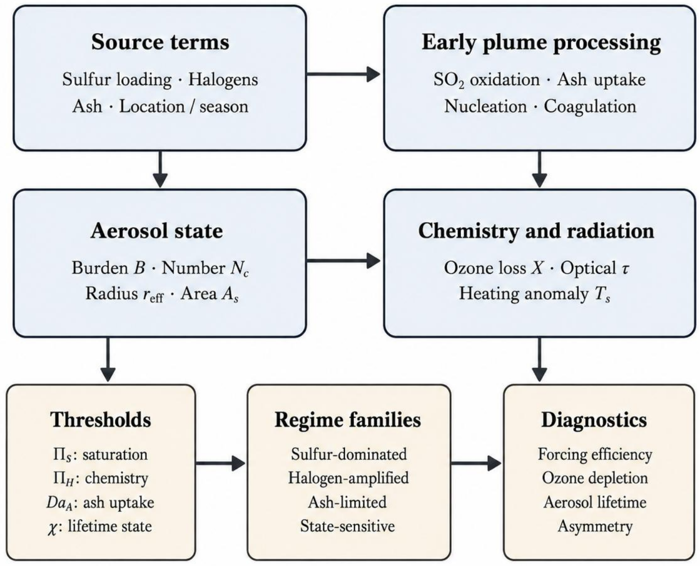

Figure 1. Conceptual architecture of the reduced-order theory. The formulation links source parameters, early plume processing, aerosol-state variables, chemistry, radiative tendencies, and circulation response. The choice of state variables and feedback pathways is motivated by the coupled sulfur–halogen–dynamics literature [2,15,16,19,20,22]. In this figure, SO_2 denotes sulfur dioxide; Π_S, Π_H, Da_A, and χ denote sulfur loading, effective halogen strength, ash-uptake Damköhler number, and lifetime-control state, respectively.

Table 1. Condensed notation used in the main text.

Symbol	Interpretation	Comment
S	Sulfur-equivalent gas-phase burden	Sulfur residing in the stratospheric sulfur dioxide (SO_2) reservoir
B	Sulfur-equivalent sulfate burden	Sulfur carried by sulfate aerosol; aerosol mass is $B_{\mathrm{aer}} = \nu_{\mathrm{sulf}} B$
N_c	Aerosol particle number column	Explicit or implicit microphysical state variable
H	Effective reactive-halogen burden	Reduced representation of chemically active chlorine and bromine
X	Fractional ozone loss	$X = 1 - \Omega/\Omega_b$
T_s	Stratospheric thermal anomaly	Net effect of aerosol heating and ozone-loss cooling
Π_S	Sulfur-loading parameter	Initial sulfate burden relative to the onset of microphysical saturation
Π_H	Halogen parameter	Effective halogen strength relative to the ozone-loss threshold
Da_A	Ash-uptake Damköhler number	Early ash scavenging relative to gas-phase oxidation
χ	Lifetime-control parameter	Signed proxy for confinement versus export in the residence-time branch
ψ	Diagnostic asymmetry coordinate	Signed proxy for partitioning toward the preferred versus opposite hemisphere

Table 2 summarizes the status, physical origin, and principal limitations of the governing equations and closures before the individual equations are introduced.

Table 2. Origin and status of the main governing equations and closures. The equation set is reduced-order by design: conservation equations encode reservoir budgets, whereas bridge laws and diagnostic relations encode physical tendencies observed in more complete studies.

Equation(s)	Status	Physical Origin or Interpretation	Main Limitation
Equations (1)–(4)	Mass-balance closure	First-order sulfur oxidation with an early ash-mediated uptake term, motivated by heterogeneous sulfur loss on ash [19]	Does not resolve ash size spectra, fall speed, or surface chemistry explicitly
Equation (5)	Reservoir budget	Conversion from gas-phase sulfur into sulfate burden and bulk removal from the stratospheric reservoir	Collapses detailed aerosol transport and removal into a single residence time
Equations (9)–(12)	Microphysical bridge law	Burden–number–radius geometry with sublinear particle-number growth under coagulation, motivated by volcanic aerosol microphysics [2,4,5]	Captures scaling and saturation, not full sectional or modal microphysics
Equations (13)–(15)	Optical/surface-area proxy closure	Geometric scaling of optical depth and surface area with burden and effective radius	Wavelength, humidity, and composition dependence are compressed into bulk constants
Equations (17)–(20)	Chemical threshold closure	Effective reactive halogen loss acting on ozone through aerosol surface area, motivated by sulfur–halogen simulations [14–16,18]	Suitable for ozone-loss thresholds, not for quantitative halogen-family partitioning
Equations (21)–(23)	Thermal and lifetime closure	Competition between aerosol heating, ozone-loss cooling, sedimentation, confinement, and self-lofting [5,20,22]	Compresses vertical structure and circulation into effective coefficients
Equations (26)–(30)	Nondimensional model	Direct scaling of the prognostic equations into a compact control space	Parameter values remain literature-informed rather than event-calibrated
Equations (38)–(40)	Regime criterion	Quasi-steady ozone-loss threshold expressed as a halogen–surface-area product	Assumes the reduced surface-area closure and a fixed chemical timescale

3.2. Sulfur Conversion with Explicit Ash Scavenging

The simplest closed representation of the early sulfur budget is a first-order sulfur-conversion closure augmented by an early ash-uptake term, consistent with published evidence for rapid heterogeneous sulfur removal on volcanic ash [19]:

$$\frac{\mathrm{d}S}{\mathrm{d}t} = -\frac{1}{\tau_{\mathrm{ox}}}\left[1 + Da_A \exp\left(-\frac{t}{\tau_{\mathrm{ash}}}\right)\right] S, \tag{1}$$

where τ_{ox} is the characteristic gas-phase oxidation timescale, and τ_{ash} is the decay timescale of the effective ash reservoir. The quantity

$$Da_A \equiv \frac{\text{initial ash-mediated sulfur loss rate}}{\text{gas-phase oxidation rate}} \tag{2}$$

is an ash-uptake Damköhler number. Equation (1) and the associated definition in Equation (2) are reduced representations of the early multiphase competition identified by [19]. Its analytical solution is

$$S(t) = S_0 \exp\left[-\frac{t}{\tau_{\mathrm{ox}}} - Da_A \frac{\tau_{\mathrm{ash}}}{\tau_{\mathrm{ox}}}\left(1 - \exp\left[-\frac{t}{\tau_{\mathrm{ash}}}\right]\right)\right]. \tag{3}$$

For $t \gg \tau_{\mathrm{ash}}$, the sulfur yield available to the sulfate aerosol is reduced by the multiplicative factor

$$Y_A \approx \exp\left(-Da_A \frac{\tau_{\mathrm{ash}}}{\tau_{\mathrm{ox}}}\right), \tag{4}$$

which provides the first explicit route by which ash modifies later forcing and chemistry in the reduced sulfur budget, again following the ash-scavenging interpretation of [19]. In the burden equation below, y_S denotes the baseline gas-to-particle conversion efficiency in the absence of ash scavenging, whereas Y_A multiplies the amount of sulfur that ultimately reaches the sulfate reservoir. In benchmark calculations, the effective sulfate yield is therefore proportional to $y_S Y_A$.

3.3. Sulfate Burden, Particle Number, and Effective Radius

The sulfate burden is governed by conversion from S and removal from the stratospheric reservoir, in line with bulk sulfur-to-sulfate aerosol budget treatments used in volcanic aerosol studies [2,4,9]:

$$\frac{\mathrm{d}B}{\mathrm{d}t} = \frac{y_S}{\tau_{\mathrm{ox}}} S - \frac{1}{\tau_{\mathrm{rem}}} B, \tag{5}$$

where $y_S \le 1$ is the baseline conversion yield and τ_{rem} is a bulk residence time to be specified below. Because both S and B are defined on a sulfur-equivalent basis, Equation (5) keeps the sulfur budget explicit while y_S remains a true conversion fraction. Whenever aerosol density or particle geometry is required below, the fixed conversion $B_{\mathrm{aer}} = \nu_{\mathrm{sulf}} B$ is applied before optical or microphysical formulas are evaluated. For diagnostic bookkeeping, the sulfur-equivalent mass not retained in the prognostic sulfate reservoir may be tracked through cumulative sinks

$$\frac{\mathrm{d}L_A}{\mathrm{d}t} = \frac{Da_A}{\tau_{\mathrm{ox}}} \exp\left(-\frac{t}{\tau_{\mathrm{ash}}}\right) S, \tag{6}$$

$$\frac{\mathrm{d}L_C}{\mathrm{d}t} = \frac{1 - y_S}{\tau_{\mathrm{ox}}} S, \tag{7}$$

$$\frac{\mathrm{d}L_R}{\mathrm{d}t} = \frac{B}{\tau_{\mathrm{rem}}}, \tag{8}$$

where L_A records ash-mediated sulfur uptake, L_C records the non-aerosolized fraction of gas-phase conversion, and L_R records removal from the sulfate reservoir. These diagnostic variables are not required to solve the reduced system, but they make explicit that $S + B + L_A + L_C + L_R$ is conserved on the sulfur-equivalent basis when no external source is added. A complete microphysical system would additionally evolve particle number through nucleation, coagulation, and dilution or export terms [2,4,6]:

$$\frac{\mathrm{d}N_c}{\mathrm{d}t} = J_n - K_c N_c^2 - \frac{1}{\tau_{\mathrm{mix}}} N_c, \tag{9}$$

with J_n a net nucleation source, K_c an effective coagulation kernel, and τ_{mix} a dilution or export timescale [2,6]. Analytical progress is facilitated by combining Equations (5) and (9) into a local scaling law that summarizes the transition from near-linear particle-number growth to coagulation-dominated saturation [4–6,8]:

$$N_c \propto B^{\beta}, \qquad 0 \le \beta \le 1, \tag{10}$$

where $\beta = 1$ corresponds to a nearly linear microphysical regime with approximately burden-independent effective radius, and $\beta \to 0$ corresponds to the saturation regime in which particle number ceases to increase materially with burden because coagulation has become dominant [4–6,8].

For an effective monodisperse representation, the particle radius follows from the geometric relation between aerosol mass, particle number, density, and effective radius [2,4]:

$$r_{\text{eff}} = \left(\frac{3B_{\text{aer}}}{4\pi\rho_p N_c} \right)^{1/3} = \left(\frac{3\nu_{\text{sulf}} B}{4\pi\rho_p N_c} \right)^{1/3}, \tag{11}$$

where ρ_p is aerosol density. Because ν_{sulf} is taken as fixed, the dimensionless burden ratios used in the bridge law below can be written equivalently in terms of B or B_{aer}. A smooth bridging law that reproduces the small-burden and large-burden asymptotes is then introduced as a reduced representation of the nonlinear radius growth seen in volcanic aerosol microphysical calculations [4–6,8]:

$$r_{\text{eff}}(B) = r_0 \left[1 + \left(\frac{B}{B_c} \right)^m \right]^{(1-\beta)/(3m)}, \tag{12}$$

where r_0 is the weak-eruption effective radius, B_c is the onset burden for microphysical saturation, β controls the large-burden particle-number response, and m controls the sharpness of the transition. Equation (12) tends to constant radius for $B \ll B_c$ and to $r_{\text{eff}} \propto B^{(1-\beta)/3}$ for $B \gg B_c$, thereby remaining consistent with the analytical scaling implied by Equation (10).

3.4. Optical Depth and Aerosol Surface Area

The aerosol optical depth at wavelength λ is

$$\tau_\lambda = Q_{\text{ext},\lambda} \pi r_{\text{eff}}^2 N_c = \frac{3Q_{\text{ext},\lambda} B_{\text{aer}}}{4\rho_p r_{\text{eff}}} = \frac{3Q_{\text{ext},\lambda} \nu_{\text{sulf}} B}{4\rho_p r_{\text{eff}}}, \tag{13}$$

where $Q_{\text{ext},\lambda}$ is the extinction efficiency [2]. The corresponding column-integrated aerosol surface area is

$$A_s = 4\pi r_{\text{eff}}^2 N_c = \frac{3B_{\text{aer}}}{\rho_p r_{\text{eff}}} = \frac{3\nu_{\text{sulf}} B}{\rho_p r_{\text{eff}}}. \tag{14}$$

Equations (13) and (14) show that the radiative branch and the heterogeneous-chemistry branch are controlled by the same ratio $B_{\text{aer}}/r_{\text{eff}}$. This identity is central: any process that changes particle size at a fixed sulfate-aerosol burden changes both radiative forcing efficiency and chemical reaction capacity.

For later use, a shortwave optical-depth proxy is defined by

$$\tau_{\text{sw}}(B) = \tau_\star \frac{B/B_\star}{\left[1 + (B/B_c)^m\right]^{(1-\beta)/(3m)}}, \tag{15}$$

with an analogous definition for $A_s(B)$ differing only by a constant prefactor. Here $B_\star$ denotes a reference sulfur-equivalent sulfate burden, $\tau_\star$ the corresponding optical-depth scale, and $A_\star = 3\nu_{\text{sulf}} B_\star / (\rho_p r_0)$ the associated reference aerosol-surface-area scale. Because $B_{\text{aer}}/B_{\text{aer},\star} = B/B_\star$ for fixed ν_{sulf}, the bridge-law proxies can be written compactly in terms of the sulfur-equivalent burden. This is a deliberate reduced-order closure: the shortwave optical-depth proxy and the heterogeneous surface-area proxy are assumed to share the same nonlinear dependence on burden and to differ only by normalization constants. The formulation does not claim to preserve the full wavelength- and size-dependent optical problem. It is most likely to break down for broad size distributions, or whenever wavelength dependence, aerosol composition, or humidity materially decouple optical-depth and surface-area proxies. The parameter

$$\Pi_S \equiv \frac{B_0}{B_c} \tag{16}$$

will serve as the dimensionless sulfur-loading parameter relative to the onset of microphysical saturation.

3.5. Reactive Halogens and Ozone Loss

A minimal effective-halogen budget is

$$\frac{\mathrm{d}H}{\mathrm{d}t} = -\frac{H}{\tau_H}, \tag{17}$$

where τ_H is the characteristic timescale over which the reactive halogen perturbation decays by sequestration, mixing, or chemical recovery [15,16]. Let $\Omega(t)$ be column ozone and define

$$X(t) \equiv 1 - \frac{\Omega(t)}{\Omega_b}, \qquad 0 \leq X \leq 1. \tag{18}$$

A reduced heterogeneous-chemical closure is then written as

$$\frac{\mathrm{d}X}{\mathrm{d}t} = k_X H A_s(B)\,[1 - X] - \frac{X}{\tau_O}, \tag{19}$$

where k_X is an effective heterogeneous-activation coefficient and τ_O is an ozone recovery timescale. Equation (19) condenses the chemically complex behavior documented in volcanic-ozone studies into a single threshold variable depending on halogen availability and aerosol surface area [14–17]. If B and H vary slowly relative to τ_O, the quasi-steady solution is

$$X^* = \frac{\Lambda}{1 + \Lambda}, \qquad \Lambda \equiv k_X \tau_O H A_s(B). \tag{20}$$

The parameter Λ identifies the chemically amplified regime. Small Λ yields weak ozone loss; $\Lambda \gtrsim 1$ yields order-one depletion. Equation (20) is used below as a diagnostic threshold relation; the time integrations in Section 6 solve the full prognostic Equation (19).

3.6. Stratospheric Thermal Tendency and Bulk Residence Time

The bulk stratospheric thermal tendency is represented as

$$\frac{\mathrm{d}T_s}{\mathrm{d}t} = \frac{\eta_a \tau_{\mathrm{sw}}(B) - \eta_O X}{C_s} - \frac{T_s}{\tau_{\mathrm{rad}}}, \tag{21}$$

where C_s is an effective stratospheric heat capacity, η_a converts aerosol optical depth into heating tendency, η_O converts ozone loss into cooling tendency, and τ_{rad} is a radiative relaxation time. Here η_a, η_O, and C_s are effective bulk coefficients whose units and interpretation absorb unresolved vertical structure, spectrally dependent radiative details, and the compressed thermodynamic structure of the reduced-order representation. Equation (21) is motivated by the competing roles of aerosol absorption and ozone-loss cooling in the stratospheric response [5,16,20]. Its quasi-steady diagnostic form is

$$T_s^* = \frac{\tau_{\mathrm{rad}}}{C_s}[\eta_a \tau_{\mathrm{sw}}(B) - \eta_O X], \tag{22}$$

which is used below only to interpret the sign of the thermal feedback. The time integrations in Section 6 solve the prognostic Equation (21) rather than imposing Equation (22) diagnostically.

The residence-time closure is written as

$$\frac{1}{\tau_{\text{rem}}} = \frac{1}{\tau_0} + a_r \left(\frac{r_{\text{eff}}}{r_0} \right)^2 - a_\chi \chi - a_T T_s, \tag{23}$$

where τ_0 is a background removal timescale, $a_r > 0$ represents enhanced sedimentation with particle size, $a_\chi > 0$ measures the dynamical contribution of the signed state parameter, and $a_T > 0$ measures the reduction of net removal by aerosol-induced lofting. In the adopted convention, positive χ increases confinement and therefore lengthens the effective residence time, whereas negative χ denotes more export-prone states. Equation (23) is intentionally bulk in form. It does not claim that all dynamical effects reduce to a single coefficient; rather, it encodes the literature-supported facts that larger particles fall faster, stronger confinement prolongs lifetime, and warming can promote lofting whereas ozone-loss cooling can counteract that mechanism [5,16,20,22]. Physically admissible states satisfy $\tau_{\text{rem}}^{-1} > 0$. The numerical integrations in Section 6 enforce this condition through a small positive lower bound, Γ_{min}, on the nondimensional removal rate. This lower bound is an admissibility regularization rather than a first-principles physical constant: it prevents nonphysical negative or vanishing removal rates in strongly confined late-tail cases. Its influence is therefore tested explicitly in the sensitivity analysis and is interpreted only as a boundary-condition uncertainty on long-tail-lifetime diagnostics.

A phenomenological hemispheric partition is also introduced through a separate diagnostic asymmetry coordinate,

$$f_P = \frac{1}{2}(1 + \tanh \psi), \qquad f_O = \frac{1}{2}(1 - \tanh \psi), \tag{24}$$

so that the hemispheric asymmetry index becomes

$$\mathcal{A}_H = \frac{B_P - B_O}{B_P + B_O} = \tanh \psi. \tag{25}$$

The subscripts P and O denote, respectively, the preferred and opposite hemisphere for a given eruption context. This representation is not intended as an exact transport law; it is a compact diagnostic map from a signed asymmetry coordinate to a bounded partition index, motivated by the strong ensemble sensitivity of hemispheric sulfur partitioning reported by [22]. The prognostic model does not require $\psi = \chi$, although that identification can be imposed later as a deliberate low-dimensional ansatz in specialized benchmark studies.

3.7. Nondimensional Form

Let

$$\hat{t} = \frac{t}{\tau_{\text{ox}}}, \qquad s = \frac{S}{S_0}, \qquad b = \frac{B}{B_0}, \qquad h = \frac{H}{H_0}, \qquad \theta = \frac{T_s}{T_\star},$$

with $B_0 = y_S S_0$ and arbitrary thermal scale $T_\star$. The nondimensional system becomes

$$\frac{\mathrm{d}s}{\mathrm{d}\hat{t}} = -\left[1 + Da_A \exp\!\left(-\frac{\hat{t}}{\hat{\tau}_{\text{ash}}} \right) \right] s, \tag{26}$$

$$\frac{\mathrm{d}b}{\mathrm{d}\hat{t}} = s - \Gamma(b, \theta, \chi) b, \tag{27}$$

$$\frac{\mathrm{d}h}{\mathrm{d}\hat{t}} = -\delta_H h, \tag{28}$$

$$\frac{\mathrm{d}X}{\mathrm{d}\hat{t}} = \Pi_H \, h \, \mathcal{A}(b) \, (1 - X) - \delta_O X, \tag{29}$$

$$\frac{\mathrm{d}\theta}{\mathrm{d}\hat{t}} = \Pi_R \, \mathcal{T}(b) - \Pi_O X - \delta_T \theta, \tag{30}$$

with

$$\hat{\tau}_{\text{ash}} = \frac{\tau_{\text{ash}}}{\tau_{\text{ox}}}, \qquad \delta_H = \frac{\tau_{\text{ox}}}{\tau_H}, \qquad \delta_O = \frac{\tau_{\text{ox}}}{\tau_O}, \qquad \delta_T = \frac{\tau_{\text{ox}}}{\tau_{\text{rad}}}, \qquad \delta_0 = \frac{\tau_{\text{ox}}}{\tau_0},$$

and

$$\mathcal{R}(b) = \left[1 + (\Pi_S b)^m\right]^{(1-\beta)/(3m)}, \qquad \mathcal{A}(b) = \frac{b}{\mathcal{R}(b)}, \qquad \mathcal{T}(b) = \frac{b}{\mathcal{R}(b)},$$

$$\Gamma(b,\theta,\chi) = \delta_0 + \alpha_r\,\mathcal{R}(b)^2 - \alpha_\chi \chi - \alpha_T \theta, \qquad \alpha_r = a_r \tau_{\text{ox}}, \qquad \alpha_\chi = a_\chi \tau_{\text{ox}}, \qquad \alpha_T = a_T T_\star \tau_{\text{ox}},$$

with

$$\Pi_H = k_X \tau_{\text{ox}} H_0 A_\star, \qquad \Pi_R = \frac{\eta_a \tau_\star \tau_{\text{ox}}}{C_s T_\star}, \qquad \Pi_O = \frac{\eta_O \tau_{\text{ox}}}{C_s T_\star}.$$

Here $A_\star$ is the reference aerosol surface-area scale introduced below Equation (15), $\mathcal{R}(b)$ is the generalized radius bridge law, $\mathcal{A}(b)$ the normalized aerosol surface-area function, and $\mathcal{T}(b)$ is the corresponding optical-depth proxy. In the present closure, $\mathcal{A}(b)$ and $\mathcal{T}(b)$ share exactly the same nonlinear dependence $b/\mathcal{R}(b)$ and differ only by constant normalization factors. The exponent β enters the strong-burden asymptote through $\mathcal{R}(b) \propto b^{(1-\beta)/3}$, thereby making the nondimensional closure consistent with the analytical scaling developed in Section 4.

The four most informative control parameters are therefore

1. $\Pi_S = B_0/B_c$: sulfur loading relative to microphysical saturation,
2. Π_H: effective halogen burden relative to the ozone-loss threshold,
3. Da_A: early ash scavenging strength,
4. χ: signed dynamical state parameter.

Much of the complexity of the full chemistry–climate problem can be understood as navigation through the $(\Pi_S, \Pi_H, Da_A, \chi)$ space.

For ease of navigation, Table 3 distinguishes among the quantities that are advanced prognostically, those used diagnostically, the closure functions that define the reduced model, and the benchmark-only quantities used for heuristic regime placement.

Table 3. Compact guide to the main layers of the reduced-order formulation.

Category	**Quantities**	**Role in the Manuscript**
Prognostic variables	s, b, h, X, θ	Advanced explicitly in time by Equations (26)–(30).
Diagnostic relations	X^*, T_s^*, $\mathcal{A}_H = \tanh\psi$	Used to interpret thresholds, thermal sign, and hemispheric partitioning without being solved prognostically in Section 6.
Closure functions	$\mathcal{R}(b)$, $\mathcal{A}(b)$, $\mathcal{T}(b)$, $\Gamma(b,\theta,\chi)$	Define the reduced microphysical, chemical, radiative, and lifetime closures of the model.
Benchmark-only quantities	$\widetilde{\Pi}_S$, benchmark sectors introduced below, and the worked ranges in Appendix D	Used only for heuristic literature placement in regime space; they are not advanced by the prognostic integrations of Section 6.

Table 4 summarizes the principal assumptions and validity limits that accompany this reduction.

Table 4. Core assumptions and intended validity of the reduced-order analysis.

Assumption	Role in the Analysis	Main Limitation
Sulfur-equivalent burden basis	Keeps the gas-phase and aerosol sulfur budget explicit while allowing a fixed conversion to dry sulfate-aerosol mass for optical and geometric relations	Does not resolve evolving sulfate composition or water uptake explicitly
Bridge-law microphysics	Represents the transition from quasi-linear particle-number growth to coagulation-dominated effective-radius growth	Does not replace sectional or modal aerosol microphysics
Shared optical-depth/surface-area nonlinearity	Allows analytical coupling between radiative and heterogeneous-chemical branches through the common ratio $B_{\mathrm{aer}}/r_{\mathrm{eff}}$	Quantitative thresholds may shift if humidity, composition, or broad size spectra decouple A_s and $\tau_{\mathrm{sw}}(B)$
Single effective halogen variable	Captures threshold behavior of heterogeneous ozone loss in a transparent form	Does not predict detailed chlorine, bromine, nitrogen, or HO_x partitioning
Bulk lifetime parameter χ	Encodes confinement/export tendency in the residence-time branch	Does not predict the circulation from first principles and must be interpreted as a low-dimensional state proxy

4. Results: Analytical Regime Theory

4.1. General Burden-Size Scaling

Assume locally that $N_c \propto B^{\beta}$ with $0 \leq \beta \leq 1$. From Equation (11),

$$r_{\mathrm{eff}} \propto \left(\frac{B}{N_c}\right)^{1/3} \propto B^{(1-\beta)/3}. \tag{31}$$

Substitution into Equation (13) yields

$$\tau_{\lambda} \propto \frac{B}{r_{\mathrm{eff}}} \propto B^{(2+\beta)/3}, \tag{32}$$

and from Equation (14),

$$A_s \propto B^{(2+\beta)/3}. \tag{33}$$

Several immediate consequences follow:

1. If $\beta = 1$, then $r_{\mathrm{eff}} \propto B^0$ and $\tau_{\lambda} \propto B$, which is the quasi-linear regime.
2. If $\beta = 0$, then $r_{\mathrm{eff}} \propto B^{1/3}$ and $\tau_{\lambda} \propto B^{2/3}$, which is the saturation regime.
3. The same burden dependence controls both optical depth and heterogeneous chemical capacity.

Thus, the additional forcing obtained per unit sulfur,

$$\eta_F \equiv \frac{|\mathrm{ERF}|}{E_S}, \tag{34}$$

must decline as

$$\eta_F \propto E_S^{(\beta-1)/3} \tag{35}$$

if B remains proportional to the sulfur yield entering the sulfate reservoir. In the saturation limit $\beta \to 0$, forcing efficiency scales as $E_S^{-1/3}$. This formal result provides an analytical counterpart to the saturation seen in large-eruption model studies [4,7,8].

4.2. Sedimentation and Residence-Time Scaling

Stokes settling gives, to the leading order,

$$v_s \approx \frac{2\rho_p g r_{\mathrm{eff}}^2 C_c}{9\mu}, \tag{36}$$

where μ is dynamic viscosity and C_c is the Cunningham correction factor. The sedimentation timescale over scale height H_s is

$$\tau_{\mathrm{sed}} \sim \frac{H_s}{v_s} \propto r_{\mathrm{eff}}^{-2} \propto B^{-2(1-\beta)/3}. \tag{37}$$

Therefore, once $\beta < 1$, increasing sulfur burden not only yields sublinear optical-depth growth but also shortens the sedimentation timescale. The two effects cooperate to produce saturation. The intuition often invoked qualitatively in the literature thereby receives a compact scaling proof [4–6].

4.3. Threshold for Chemically Amplified Ozone Depletion

From Equation (20), strong ozone loss begins when $\Lambda \gtrsim 1$, that is,

$$k_X \tau_O H A_s(B) \gtrsim 1. \tag{38}$$

Using Equation (33),

$$\Lambda \propto H B^{(2+\beta)/3}. \tag{39}$$

If H is written in terms of the effective halogen parameter Π_H, then the chemical threshold becomes

$$\Lambda \sim \Pi_H \Pi_S^{(2+\beta)/3}. \tag{40}$$

The result is noteworthy. Even when the forcing efficiency per sulfur declines in the saturation regime, the aerosol surface area can still remain large enough to support severe halogen activation. In other words, super-eruption chemical hazard need not saturate in the same manner as incremental radiative forcing. This provides a theoretical basis for the large ozone losses found in halogen-rich super-eruption simulations [15,16,18].

4.4. Ash Scavenging Shifts Both Radiative and Chemical Thresholds

If early ash scavenging reduces the sulfur yield by the factor Y_A from Equation (4), then all burden-controlled thresholds shift. For the radiative branch,

$$\tau_\Lambda \propto (Y_A E_S)^{(2+\beta)/3}, \tag{41}$$

while forcing efficiency scales as

$$\eta_F \propto Y_A^{(2+\beta)/3} E_S^{(\beta-1)/3}. \tag{42}$$

For the chemical branch,

$$\Lambda \propto \Pi_H (Y_A E_S)^{(2+\beta)/3}. \tag{43}$$

Ash therefore moves the system diagonally in regime space. It reduces the sulfate burden and the aerosol surface area simultaneously, potentially displacing a super-eruption from a chemically amplified regime back toward a sulfur-dominated regime. Because the dependence is sublinear, the resulting reduction in forcing or ozone loss is weaker than a one-to-one loss of sulfur mass would suggest, but it remains dynamically and chemically important [19].

4.5. Competition Between Aerosol Heating and Ozone-Loss Cooling

Equation (22) implies the thermal control ratio

$$\Theta \equiv \frac{\eta_O X}{\eta_a \tau_{\mathrm{sw}}(B)}. \tag{44}$$

If $\Theta < 1$, aerosol heating dominates and the volcanic cloud is predisposed toward self-lofting and prolonged residence. If $\Theta > 1$, ozone-loss cooling dominates and the self-lofting tendency is suppressed. Combined with Equation (23), the sign of the thermal feedback becomes

$$\frac{\partial \tau_{\mathrm{rem}}}{\partial X} = a_T \tau_{\mathrm{rem}}^2 \frac{\partial T_s}{\partial X} \approx -\frac{a_T \tau_{\mathrm{rad}} \eta_O}{C_s} \tau_{\mathrm{rem}}^2 < 0 \tag{45}$$

if the direct size-mediated dependence of τ_{sw} on X is neglected. Under that approximation, stronger ozone loss shortens the residence time by cooling the stratosphere. The same mechanism underlies the forcing amplification by sulfur–halogen co-emission found in comprehensive modeling [16].

4.6. State Dependence and Hemispheric Asymmetry

From Equation (25), the hemispheric asymmetry index is bounded and monotonic in the diagnostic coordinate ψ:

$$-1 < \mathcal{A}_H = \tanh \psi < 1. \tag{46}$$

This formal choice is advantageous because it prevents unrealistically unbounded asymmetry while preserving interpretability. Small $|\psi|$ corresponds to nearly symmetric partitioning, whereas large positive or negative ψ denotes preferential partitioning toward the preferred or opposite hemisphere. Bulk lifetime sensitivity is governed separately by χ through Equation (23). The present formulation therefore allows asymmetry and lifetime to vary independently when the literature suggests decoupling, while still permitting the optional identification $\psi = \chi$ in benchmark contexts where both tend to covary. Figure 2 visualizes the resulting saturation scalings, Figure 3 shows the chemically amplified regime in the (Π_S, Π_H) plane, and Figure 4 illustrates the separate asymmetry and lifetime-control diagnostics.

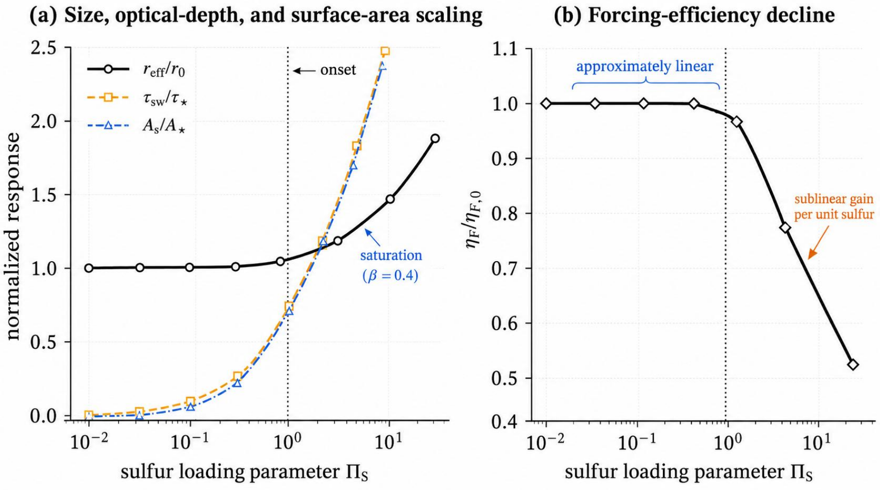

Figure 2. Analytical scaling behavior implied by the reduced-order theory for a representative intermediate microphysical exponent ($\beta = 0.4$). Panel (**a**) shows how the generalized bridge law produces simultaneous growth in effective radius, optical depth, and aerosol surface area as the system crosses the saturation threshold. Panel (**b**) shows the associated decline in forcing efficiency. The highlighted transition corridor is motivated by the quasi-linear window identified by [7], whereas the sublinear asymptote is consistent with the saturation behavior discussed by [4,8].

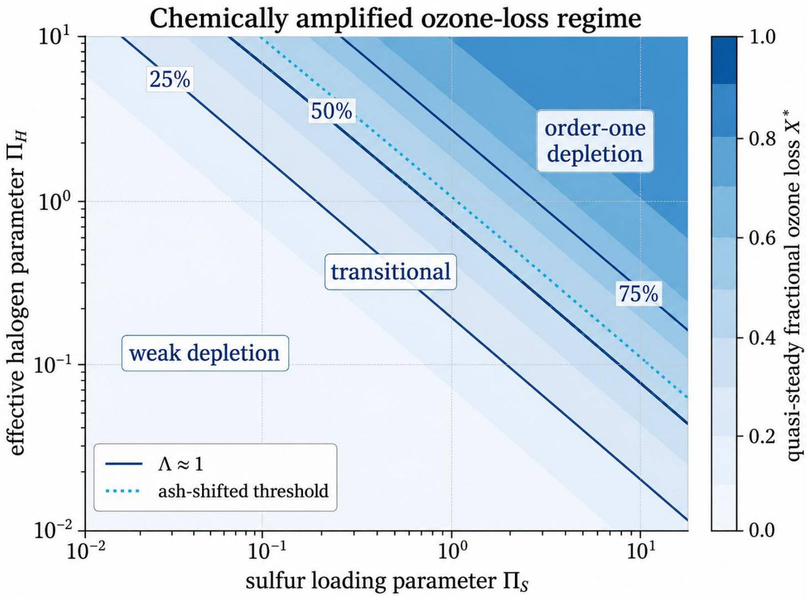

Figure 3. Illustrative ozone-loss regime map implied by Equation (20). The color scale shows the quasi-steady ozone-loss fraction X^* as a function of sulfur loading and effective reactive-halogen burden. Solid contours indicate 25%, 50%, and 75% ozone loss. The dashed and dotted threshold curves mark, respectively, the unmodified and ash-shifted $\Lambda \approx 1$ boundaries. The figure emphasizes that ozone loss is jointly controlled by aerosol surface area and reactive halogen availability [15–19].

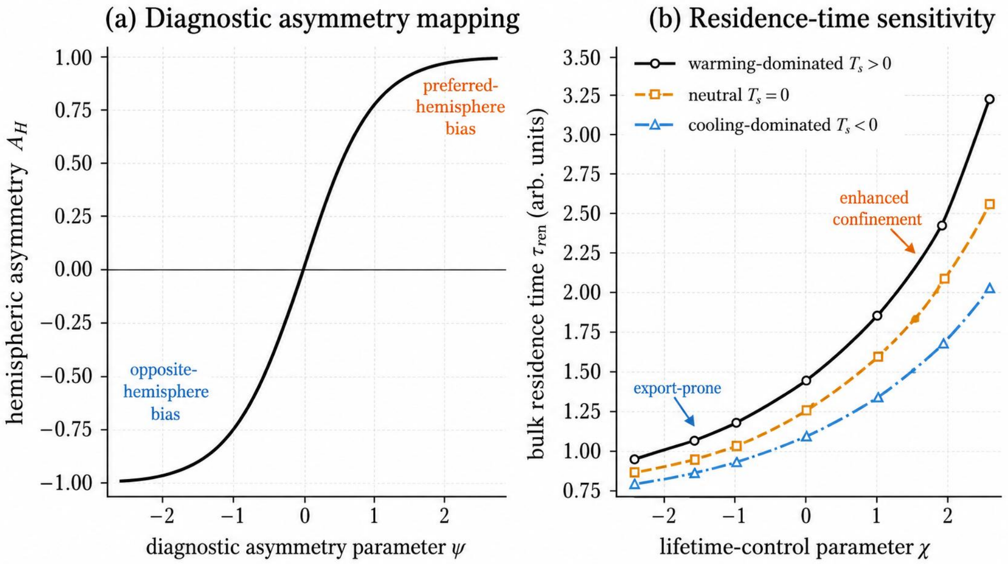

Figure 4. Illustrative dynamical metrics associated with the revised low-dimensional formulation. Panel (**a**) maps the diagnostic asymmetry coordinate ψ onto hemispheric asymmetry through Equation (25). Panel (**b**) shows a representative dependence of bulk residence time on the stratospheric thermal anomaly and the lifetime-control parameter χ using the sign convention adopted in Equation (23), for which positive χ denotes enhanced confinement. The purpose is not to replace resolved dynamics but to expose the types of sensitivity documented for jet response, QBO perturbation, and initial-condition dependence in comprehensive models [20,22–24].

5. Results: Literature-Anchored Parameter Benchmarking

5.1. Transparent Mapping from Published Quantities to Control Parameters

The reduced-order variables are dimensionless by construction, but their plausible ranges can still be anchored to the eruption literature through transparent order-of-magnitude mappings. The purpose of the present section is not to claim a formal inversion for any one event. It is to show explicitly how sulfur mass, halogen effectiveness, ash-mediated sulfur suppression, and circulation state can be translated into the reduced control space with uncertainty ranges [7,8,10,15,18,19,22]. The resulting benchmark placements should therefore be read as interpretive, heuristic regime placements within the reduced-order control space rather than as calibrated event estimates, inverse-retrieved constraints, or quasi-empirical estimates. Sulfur loading and ash suppression are constrained most directly by literature estimates of E_S, Y_A, and the transition-scale $E_{S,c}$, whereas Π_H, χ, and, where used, ψ retain a stronger theory-mediated component because they organize published ozone-loss and transport-state information within the reduced-order control space.

To avoid conflating benchmark placement with prognostic integration, the benchmark sulfur coordinate is written here as an *effective post-ash loading*,

$$\widetilde{\Pi}_S \approx \frac{(y_S/y_{S,\mathrm{ref}})Y_A E_S}{E_{S,c}}, \tag{47}$$

where E_S is injected sulfur mass, y_S is the baseline gas-to-particle conversion yield from Equation (5), $y_{S,\mathrm{ref}}$ is the reference yield used to define the benchmark onset scale, and $E_{S,c}$ is the sulfur amount associated with the onset of microphysical saturation for that reference yield. Guided by the transition corridor isolated by [7] and the saturation study of [8], $E_{S,c}$ is interpreted here as an order-of-magnitude threshold rather than a universal constant. In the worked benchmark ranges below, y_S is taken to be close to $y_{S,\mathrm{ref}}$, so the practical placements reduce to the compact working form $\widetilde{\Pi}_S \approx Y_A E_S/E_{S,c}$ used in the supplementary sheet. The symbol $\widetilde{\Pi}_S$ is used only for heuristic benchmark placement after ash suppression. By contrast, the illustrative integrations in Section 6 hold a nominal pre-ash loading $\Pi_S^{(0)}$ fixed and treat ash dynamically through Da_A, so the effective loading emerges prognostically rather than being prescribed.

The halogen parameter can be related to the quasi-steady ozone threshold through

$$\Pi_H \approx \frac{\Lambda_{\mathrm{ref}}}{\widetilde{\Pi}_S^{(2+\beta_{\mathrm{ref}})/3}}, \qquad \Lambda_{\mathrm{ref}} \approx \frac{X_{\mathrm{ref}}}{1-X_{\mathrm{ref}}}, \tag{48}$$

where X_{ref} is a representative ozone-loss fraction inferred from published sulfur–halogen simulations and β_{ref} is a representative intermediate microphysical exponent. Equation (48) makes explicit that the same reported ozone loss implies different effective Π_H values depending on the benchmark-effective sulfur-loading regime.

Ash influence can be translated into the reduced model through the ash-suppressed sulfur yield,

$$Da_A \approx -\frac{\tau_{\mathrm{ox}}}{\tau_{\mathrm{ash}}}\ln Y_A, \tag{49}$$

which follows directly from Equation (4). Lifetime control and asymmetry are then treated separately. When published diagnostics permit an explicit hemispheric partition estimate, the asymmetry coordinate is obtained from

$$\psi \approx \operatorname{arctanh}(\mathcal{A}_H). \tag{50}$$

By contrast, χ is assigned as a bounded dynamical-state class inferred from season, latitude, and initial-condition sensitivity: export-prone states correspond to $\chi < 0$, neutral states to $\chi \approx 0$, and comparatively confined states to $\chi > 0$. In concrete tropical benchmark contexts, the preferred hemisphere denotes the hemisphere toward which the initial circulation state biases early net export, whereas the opposite hemisphere denotes the complementary branch. Concrete adopted ranges for all input and output quantities are listed in

Appendix D and in the Supplementary Benchmark Calculation Sheet. Table 5 summarizes the mappings used to translate literature quantities into reduced-order control parameters.

Table 5. Transparent order-of-magnitude mappings between published eruption characteristics and reduced-order control parameters.

Parameter	**Working Mapping**	**Literature Inputs Used for Benchmarking**
$\widetilde{\Pi}_S$	$\widetilde{\Pi}_S \approx Y_A E_S / E_{S,c}$	Injected sulfur mass E_S, ash-suppressed sulfate yield Y_A, and a saturation-onset scale $E_{S,c}$ informed by the 10–40 Tg S transition corridor and large-eruption saturation studies
Π_H	$\Pi_H \approx \Lambda_{\text{ref}} / \widetilde{\Pi}_S^{(2+\beta_{\text{ref}})/3}$ with $\Lambda_{\text{ref}} \approx X_{\text{ref}} / (1 - X_{\text{ref}})$	Published ozone-loss fraction, reactive halogen delivery efficiency, and a representative microphysical exponent
Da_A	$Da_A \approx -(\tau_{\text{ox}}/\tau_{\text{ash}}) \ln Y_A$	Early sulfur-yield suppression inferred from ash-mediated uptake estimates
χ	Assigned as a bounded dynamical-state class inferred from season, latitude, and initial-condition sensitivity	Reported transport sensitivity, preferred confinement/export tendency, and eruption-context diagnostics
ψ	$\psi \approx \operatorname{arctanh}(\mathcal{A}_H)$ when an asymmetry estimate is reported	Hemispheric aerosol asymmetry or equivalent partition diagnostics

Table 6 gives the operational classification used to assign the reduced dynamical-state parameter χ in a reproducible way.

Table 6. Standardized dynamical-state classification used to assign the lifetime-control coordinate χ. The classes are intentionally coarse and reproducible: they encode the expected direction of the residence-time effect rather than a resolved circulation simulation.

Class	**Adopted χ Band**	**Diagnostic Criteria**	**Interpretation**
Export-prone	-0.6 to -0.1	Published or expected early export from the main aerosol reservoir, weak confinement, or strong cross-equatorial dilution	Shorter effective residence time
Neutral	-0.1 to $+0.1$	No strong evidence for preferential confinement or export, or insufficient dynamical information	Background residence-time branch
Weakly confined	$+0.1$ to $+0.3$	Initial-state or seasonal context favors slower export or partial hemispheric retention	Moderately prolonged residence time
Confined	$+0.3$ to $+0.6$	Published simulations or eruption context indicate strong confinement, delayed export, or persistent reservoir retention	Long-tail residence-time sensitivity

5.2. Benchmark Placement of Representative Eruption Classes

Figure 5 and Table 7 show the resulting heuristic benchmark sectors for representative eruption classes in the $(\widetilde{\Pi}_S, \Pi_H)$ plane. The rectangular sectors in Figure 5 are uncertainty boxes rather than best-fit points. They indicate the range obtained when published sulfur release, ozone depletion, ash influence, and transport-state information are propagated through Equations (47)–(49) together with the dynamical-state and asymmetry assignments described above. Additional construction details, adopted input ranges, and interpretive envelopes are reported in Appendix D (Tables A2 and A3) and in the document entitled Supplementary Benchmark Calculation Sheet, which is included with the Supplementary Materials in PDF and CSV form. The important point is not the exact coordinate assigned to any one event; it is that the analytical thresholds intersect recognizable eruption classes already studied with comprehensive models, while still remaining clearly interpretive, heuristic regime placements rather than calibrated event estimates, inverse-retrieved constraints, or quasi-empirical estimates.

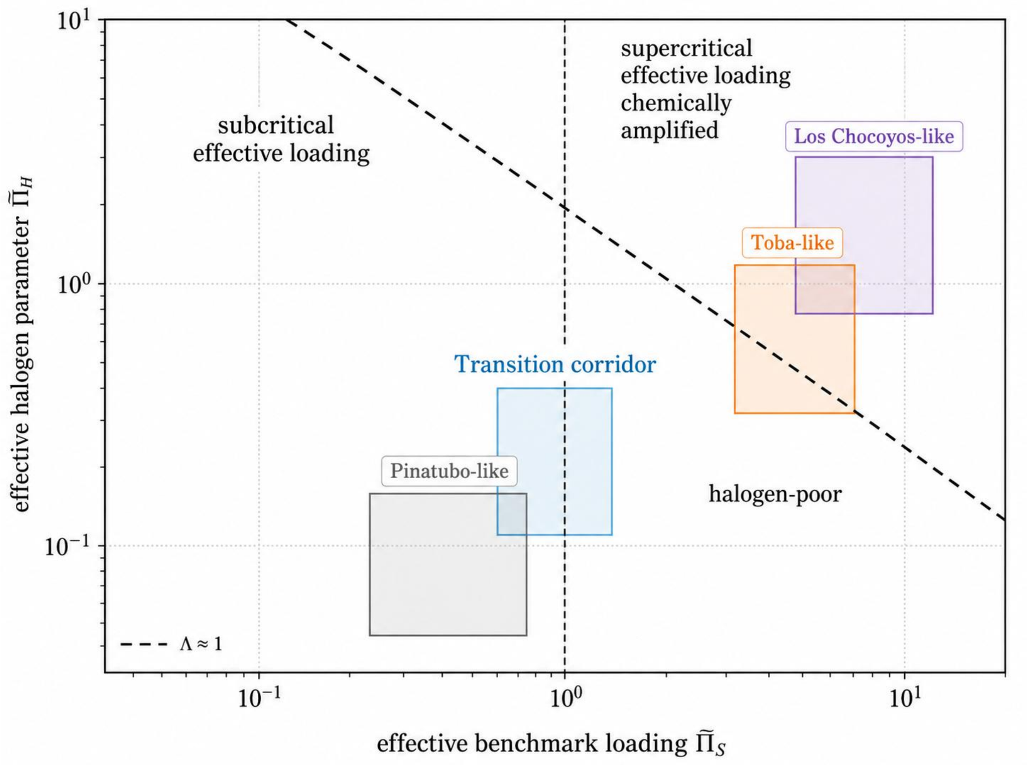

Figure 5. Literature-anchored placement of representative eruption classes in the $(\widetilde{\Pi}_S, \Pi_H)$ plane. The vertical dashed line marks the onset of microphysical saturation at $\widetilde{\Pi}_S \sim 1$, while the sloping dashed line approximates the chemical-amplification threshold $\Lambda \sim 1$ for a representative intermediate microphysical exponent. Boxes indicate interpretive, heuristic regime placements and uncertainty sectors rather than calibrated event estimates, fitted points, inverse-retrieved constraints, or quasi-empirical estimates. Additional construction details are provided in Appendix D and in the Supplementary Benchmark Calculation Sheet included with the Supplementary Materials.

Table 7. Representative eruption-class placements inferred from the transparent benchmark mappings. Ranges denote interpretive, heuristic uncertainty sectors in $(\widetilde{\Pi}_S, \Pi_H)$ space rather than calibrated event estimates or inverse solutions for specific eruptions.

Eruption Class	Benchmark Sector	Interpretation Within the Reduced Theory	Principal Literature Basis
Pinatubo-like	$\widetilde{\Pi}_S \approx 0.3$–$0.8$, $\Pi_H \lesssim 0.1$, negligible Da_A	Near-quasi-linear sulfate response, limited chemical amplification, and residence-time sensitivity dominated by ordinary transport variability	[1,10,11,13]
Idealized 10–40 Tg S tropical corridor	$\widetilde{\Pi}_S \approx 0.6$–$1.2$, low-to-moderate Π_H, negligible Da_A	Transition from approximately linear scaling toward saturation; useful corridor for locating the onset of nonlinearity	[7,8]
Toba-like	$\widetilde{\Pi}_S \approx 3$–$6$, $\Pi_H \approx 0.2$–0.6, modest Da_A, state-sensitive χ	Saturated forcing efficiency, large aerosol surface area, and marked ozone vulnerability without requiring extreme Π_H	[4,18,24,25]
Los Chocoyos-like	$\widetilde{\Pi}_S \approx 4$–$7$, $\Pi_H \approx 0.5$–1.6, $Da_A \approx 0.3$–1.0, state-sensitive χ	Strong chemical amplification, ash-modified sulfur yield, substantial ozone depletion, and pronounced sensitivity to transport history	[15,19,22,26]

Table 8 provides a semi-quantitative consistency check against representative anchor cases, without converting the reduced theory into an event-calibrated model.

Table 8. Semi-quantitative anchor-case consistency check. The table does not calibrate the model to particular events; it records whether the reduced theory reproduces the qualitative ordering of regime behavior reported in representative modeling and observational studies.

Anchor Class	**Literature Behavior Used as Qualitative Target**	**Behavior Produced by the Reduced Theory**	**Consistency Level**
Pinatubo-like	Near-linear optical response, moderate lifetime, limited halogen amplification unless halogen delivery is unusually efficient [1,10,11]	Below or near the saturation threshold, weak chemical amplification, and transport-dominated lifetime variability	High for regime ordering
10–40 Tg S tropical corridor	Approximately scalable temperature and precipitation anomalies over a finite moderate-loading range, approaching saturation at upper loadings [7,8]	Transition sector near $\widetilde{\Pi}_S \sim 1$, where the bridge law begins to depart from linear optical scaling	High for onset behavior
Toba-like	Large sulfur loadings, forcing-efficiency saturation, strong ozone vulnerability under halogen-rich assumptions, and strong dynamical sensitivity in models [4,18,24,25]	Supercritical sulfur loading, sublinear forcing efficiency, and strong chemical response only when Π_H approaches an order of unity	Moderate to high; event details remain model-dependent
Los Chocoyos-like	Sulfur- and halogen-rich forcing, substantial ozone depletion in chemistry–climate simulations, ash-mediated sulfur loss, and contested long-duration climate expression [15,19,26]	Chemically amplified, ash-modified sector with strong short-lived chemical disruption but non-proportional radiative scaling	High for qualitative regime logic; not an event reconstruction

5.3. External Consistency Against Published Eruption Responses

The benchmark sectors above are not a validation in themselves, because their coordinates are constructed from the same literature used to define representative eruption classes. A separate external-consistency check was therefore added to test whether the reduced theory reproduces the expected rank ordering of independent published diagnostics. The comparison is deliberately semi-quantitative: the target is not pointwise agreement with any single three-dimensional simulation but consistency with the published ordering of aerosol saturation, forcing-efficiency decline, chemically amplified ozone loss, ash-modified sulfur yield, and residence-time sensitivity across eruption classes.

A formal pointwise error estimate against three-dimensional chemistry–climate simulations is therefore not assigned. Such an estimate would require event-specific emissions, injection geometry, season, latitude, meteorological state, aerosol microphysics, and halogen chemistry to be specified in a fully coupled spatial model, and the present theory is not calibrated as a surrogate for any individual three-dimensional model. External consistency is instead assessed through regime membership, sign of response, rank ordering, and broad magnitude behavior. This criterion is appropriate for the intended use of the model as an organizing theory and experiment-design tool, rather than as a predictor of absolute aerosol optical depth, forcing, ozone loss, or temperature.

Table 9 summarizes this check. The reduced theory reproduces the expected progression from Pinatubo-like behavior, through the idealized 10–40 Tg S transition corridor, toward sulfur-saturated and chemically amplified super-eruption sectors. It also separates the ash-mediated early sulfur-yield effect from the dynamical late-tail residence-time effect. This comparison should be read as an external plausibility test of regime topology, not as a calibration of numerical amplitudes or a validation against resolved three-dimensional fields.

Table 9. External consistency check against published eruption-response classes. The check evaluates rank ordering and approximate regime behavior rather than event-specific amplitudes.

Diagnostic Target	Published Behavior Used as External Target	Reduced-Order Behavior Without Event-Specific Recalibration	Consistency Assessment
Aerosol size and forcing efficiency	Pinatubo-like cases remain near the quasi-linear regime, whereas Toba-like and larger idealized eruptions produce larger particles and declining forcing efficiency [4,7,8]	$\Pi_S < 1$ yields weak radius growth; $\Pi_S > 1$ produces sublinear optical-depth scaling and declining η_F	Correct rank ordering of forcing-efficiency loss
Moderate 10–40 Tg S corridor	Published ensembles indicate approximate scalability over a finite tropical corridor, not unlimited linearity [7]	The corridor lies near the transition into saturation rather than deep in the supercritical regime	Consistent transition behavior
Halogen-rich ozone loss	Los Chocoyos-like and Toba-like sulfur–halogen simulations show substantially stronger ozone depletion than sulfur-only scaling would imply [15,16,18]	The threshold $\Pi_H \mathcal{A}(b) \gtrsim 1$ moves high-surface-area, halogen-rich cases into a chemically amplified regime	Correct chemical-amplification ordering
Ash-mediated sulfur suppression	Persisting ash can remove a substantial fraction of sulfur before complete sulfate formation [19]	Increasing Da_A lowers the effective loading coordinate and reduces the integrated optical-depth proxy at fixed nominal loading	Consistent sign and early-phase timing
Dynamical persistence	Initial state, season, and transport history alter hemispheric partitioning and aerosol lifetime in comprehensive models [20,22,23]	Positive χ lengthens the late-tail response while ψ diagnoses hemispheric partitioning independently	Consistent direction of state dependence

6. Results: Illustrative Reduced-Order Integrations

6.1. Computational Implementation and Scenario Design

Section 6 uses the reduced theory in a prognostic mode. The integrations therefore hold a nominal pre-ash loading $\Pi_S^{(0)}$ fixed and evolve ash effects dynamically through the uptake term and Da_A. This differs intentionally from the benchmark sectors in Section 5, which employ the ash-suppressed effective loading $\widetilde{\Pi}_S$ for heuristic regime placement. The two constructions are therefore complementary rather than identical: the former is prognostic, and the latter is interpretive.

To demonstrate the behavior of the theory, the nondimensional system in Equations (26)–(30) was integrated with Python's adaptive Runge–Kutta `solve_ivp` implementation (method `RK45`, relative tolerance 10^{-7}, and absolute tolerance 10^{-9}). The prognostic initial conditions were stated explicitly as

$$s(0) = 1, \qquad b(0) = 0, \qquad h(0) = 1, \qquad X(0) = 0, \qquad \theta(0) = 0.$$

The nondimensional integrations were performed over $0 \leq \hat{t} \leq 26$. The raw removal function $\Gamma(b, \theta, \chi)$ was clipped to a minimum admissible value $\Gamma_{\min} = 0.08$ in order to prevent unphysical negative removal rates and to represent a small residual background removal that persists even in strongly lofted or confined states. This lower bound is introduced as an admissibility regularization of the reduced closure rather than as a parameter derived directly from first principles. Because this floor can affect the long tail of the decay, its influence is examined explicitly in Section 6.3. All publication figures were produced in Python using NumPy and SciPy's `solve_ivp`, and exported as vector PDF graphics using Matplotlib [32–34]. The supplementary scripts were tested with Python 3.13.5, NumPy 2.3.5, SciPy 1.17.0, and Matplotlib 3.10.8; the supplied `requirements.txt` and `environment.yml` files record the same tested environment.

The shared closure parameters used in Figure 6 were $\beta = 0.40$, $m = 2.5$, $\hat{\tau}_{\text{ash}} = 0.67$, $\delta_H = 0.055$, $\delta_O = 0.032$, $\delta_T = 0.28$, $\delta_0 = 0.58$, $\alpha_r = 0.09$, $\alpha_\chi = 0.10$, $\alpha_T = 0.16$, $\Pi_R = 1.00$, $\Pi_O = 1.00$, and $\Gamma_{\min} = 0.08$. These values are not a calibration to any one event. They were chosen to populate the analytical regime space with plausible ordering among sulfur-dominated, halogen-amplified, and ash-modified cases while keeping the closure transparent. The explicit scenario-specific parameter values are listed in Table 10 and duplicated in `scenario_table.csv` in the Supplementary Materials.

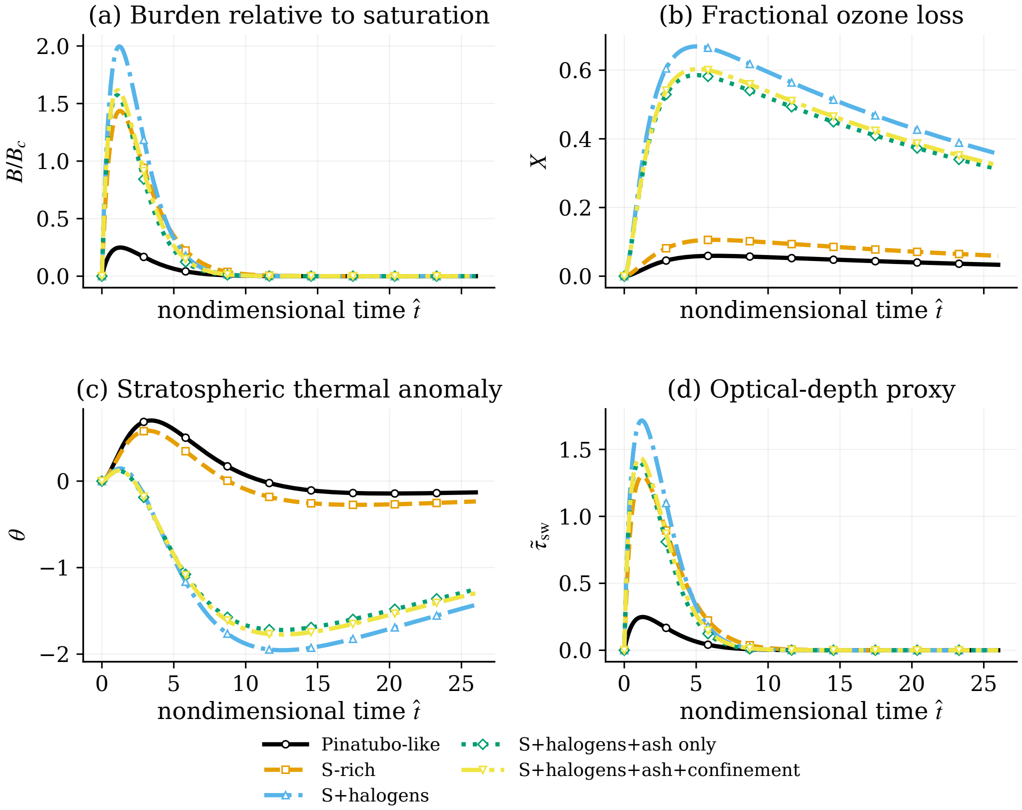

Figure 6. Illustrative reduced-order integrations for five eruption classes. Panel (**a**) shows the sulfate burden relative to the saturation threshold, panel (**b**) the fractional ozone loss, panel (**c**) the stratospheric thermal anomaly, and panel (**d**) a shortwave optical-depth proxy. The trajectories are not event reconstructions; they visualize the contrasts implied by the regime theory using the explicit parameter values listed in Table 10. In contrast to the benchmark sectors of Figure 5, these prognostic runs evolve ash effects dynamically at fixed nominal pre-ash loading $\Pi_S^{(0)}$ rather than using an ash-suppressed effective loading for placement. The ash-only and ash-plus-confinement cases are shown separately so that ash effects can be distinguished from dynamical-state effects.

Table 10. Scenario-specific parameters used for the illustrative integrations in Figure 6. The five cases share the common closure parameters listed in the text. The sulfur-loading column reports the nominal pre-ash loading $\Pi_S^{(0)}$ held fixed in the prognostic integrations.

Case	$\boldsymbol{\Pi_S^{(0)}}$	$\boldsymbol{\Pi_H}$	$\boldsymbol{Da_A}$	$\boldsymbol{\chi}$
Pinatubo-like	0.55	0.05	0.00	0.00
Sulfur-rich, halogen-poor	3.20	0.10	0.00	0.05
Sulfur-rich, halogen-rich	4.50	1.20	0.00	0.10
Sulfur-rich, halogen-rich + ash only	4.50	1.20	0.75	0.10
Sulfur-rich, halogen-rich + ash + confinement	4.50	1.20	0.75	0.55

The five-scenario sample, respectively, a near-threshold Pinatubo-like case, a sulfur-rich but chemically weak case, a chemically amplified sulfur-rich case, an ash-only perturbation relative to the chemical reference, and a combined ash-plus-confinement case. The last two are displayed separately so that the microphysical–chemical effect of early ash uptake can be distinguished from the additional dynamical effect of enhanced confinement.

6.2. Integrated Response Families

Figure 6 shows five distinct reduced-order response families. Panel (a) plots the burden relative to the microphysical-saturation threshold, B/B_c, rather than the internally normalized variable b; this makes the relation to the nominal pre-ash loading $\Pi_S^{(0)}$ explicit. Sulfur-rich cases rise above the saturation threshold, but the peak burden remains sublinear because particle growth and removal intensify together. Panel (b) shows that large sulfur loading alone does not imply severe chemical impact: order-one ozone depletion appears only when the effective halogen parameter approaches the chemically amplified regime. Panel (c) illustrates the competition between aerosol heating and ozone-loss cooling, and panel (d) shows that radiative proxy and chemical response need not peak simultaneously.

The ash-only trajectory now isolates the effect of changing Da_A at fixed χ. Relative to the sulfur-rich and halogen-rich reference case, early ash uptake reduces the burden and optical-depth proxy while leaving the event within a high-Π_H sector of parameter space. The additional ash-plus-confinement trajectory shows how that ash signal is modified when the lifetime branch is perturbed simultaneously through χ. The figure is therefore intended to separate, rather than conflate, ash-induced threshold displacement from dynamical-state effects.

6.3. Structured Sensitivity Analysis

Because several closures remain heuristic, only bounded robustness claims are appropriate at this stage. An expanded local one-at-a-time analysis was therefore performed around the reference sulfur-rich, halogen-rich case ($\Pi_S^{(0)} = 4.5$, $\Pi_H = 1.2$, $Da_A = 0.35$, $\chi = 0.2$) using centered ±20% perturbations. Four diagnostics were tracked: peak burden relative to saturation B_{pk}/B_c, peak ozone loss X_{pk}, time-integrated optical-depth proxy $I_\tau = \int \tilde{\tau}_{\rm sw}\, d\hat{t}$, and post-peak half-decay time $t_{1/2}$. Here $\tilde{\tau}_{\rm sw} \equiv \tau_{\rm sw}(B)/\tau_\star$ denotes the normalized optical diagnostic plotted in Figure 6; it is proportional to the thermal-closure input $\mathcal{T}(b)$ in Equation (30), with constant normalization absorbed into Π_R, but the two symbols are kept distinct because $\mathcal{T}(b)$ enters the temperature equation whereas $\tilde{\tau}_{\rm sw}$ is a reported optical proxy. The perturbation set includes both χ itself and the removal-rate floor $\Gamma_{\rm min}$.

The resulting sensitivities are shown in Figure 7. Panel (a) gives local elasticities at the reference state, whereas panels (b) and (c) provide two compact interaction tests. At the reference state used in panel (a), the admissibility floor $\Gamma_{\rm min}$ is inactive, which is why the corresponding local elasticity is essentially zero there. None of the Figure 6 trajectories reach the floor over the plotted interval; $\Gamma_{\rm min}$ becomes dynamically relevant only in more confined cases for which the raw removal function would otherwise cross the admissibility bound, so its influence is concentrated in the late decay tail illustrated in panel (c). Within the explored neighborhood of parameter space, three conclusions follow. First, X_{pk} remains controlled most strongly by Π_H, δ_O, and the generalized size-growth exponent β, confirming that the chemically amplified regime is fundamentally a sulfur–halogen–surface-area problem. Second, I_τ decreases systematically as Da_A increases, but this ash effect is partially offset when χ moves toward more confined states; the interaction is therefore real but does not overturn the primary ash signal. Third, the long-tail diagnostic $t_{1/2}$ does depend on the removal-rate floor in the most confined cases, precisely because the admissibility condition $\Gamma \geq \Gamma_{\rm min}$ becomes active there, yet the ordering of the main response families resolved within the explored neighborhood remains unchanged across the tested $\Gamma_{\rm min}$ range and chosen integration horizon. The present sensitivity analysis is therefore interpreted strictly as a local robustness check around a representative state rather than as evidence for global robustness across the full regime space. This limitation is particularly relevant for lifetime-related diagnostics, for which the most confined cases retain some dependence on both $\Gamma_{\min}$ and the chosen integration horizon through the decay tail.

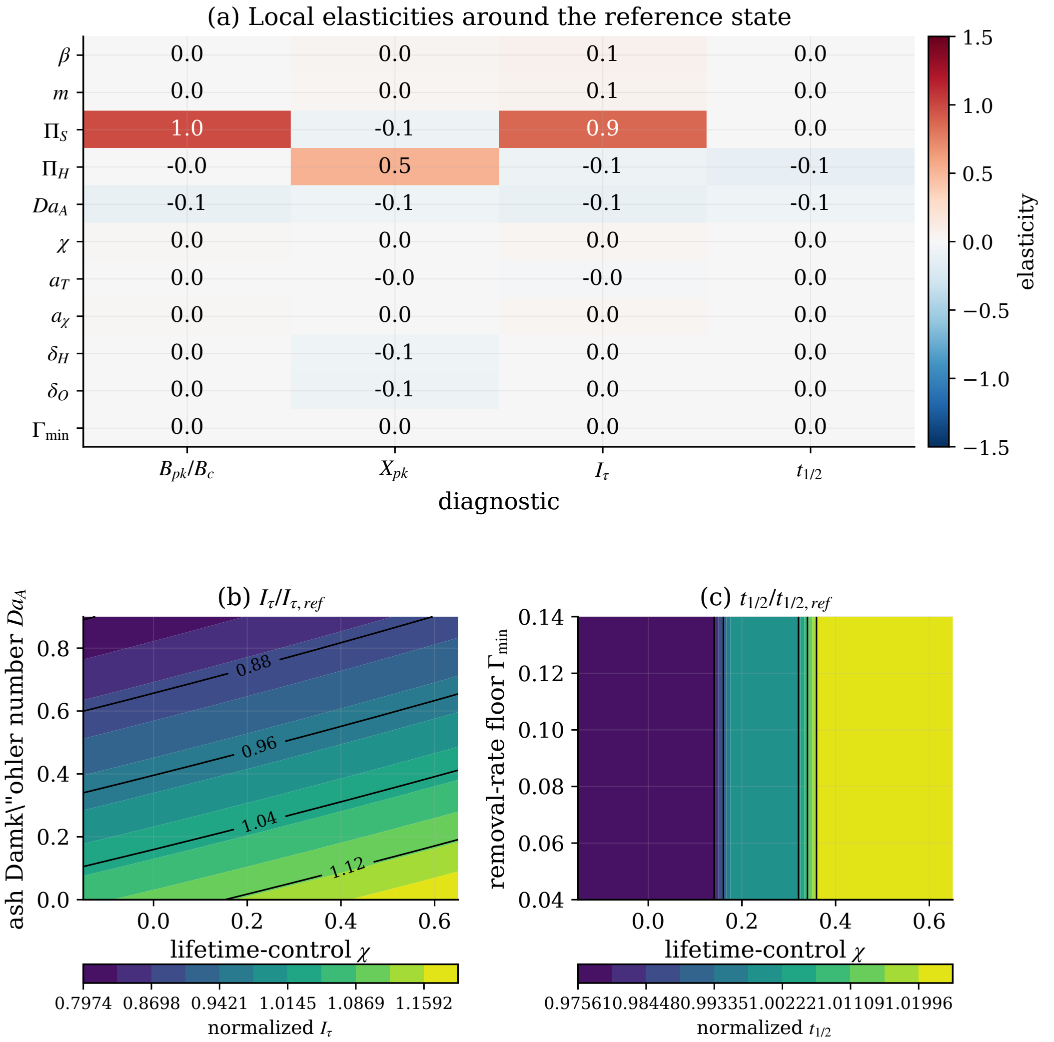

Figure 7. Expanded sensitivity analysis around the reference sulfur-rich, halogen-rich case. Panel (**a**) reports local logarithmic elasticities of four reduced-order diagnostics to eleven parameters, including χ and the removal-rate floor $\Gamma_{\min}$; $\Gamma_{\min}$ is inactive at this reference state, explaining the near-zero local elasticity of the associated early-to-intermediate diagnostics. Panel (**b**) shows how the time-integrated optical-depth proxy varies under joint perturbations of ash strength and dynamical confinement. Panel (**c**) shows how the post-peak half-decay time depends jointly on $\Gamma_{\min}$ and χ. The figure is intended as a compact local robustness check rather than as an exhaustive survey of the full regime space.

In addition to the centered ±20% local elasticities, the placement of the main threshold lines was checked against wider variations in the closure parameters most directly questioned by the reviewers. Table 11 reports the qualitative displacement implied by varying β, m, and $\Gamma_{\min}$ over broader interpretive ranges. The exponent β changes the slope of the chemical threshold through $\Pi_H \propto \widetilde{\Pi}_S^{-(2+\beta)/3}$, so the exact position of the sloping line in Figure 5 is closure-dependent. The bridge sharpness m modifies how abruptly the system crosses from quasi-linear to saturating behavior near $\widetilde{\Pi}_S \sim 1$, but it does not alter the asymptotic slopes. The removal-rate floor $\Gamma_{\min}$ does not move the chemical or microphysical threshold lines; it affects only late-tail lifetime diagnostics once the raw removal function approaches the admissibility bound.

Table 11. Broader threshold-sensitivity summary for the closure parameters most relevant to Figure 5 and the lifetime diagnostics. The entries indicate displacement of regime boundaries, not recalibrated event estimates.

Parameter	Tested Range	Effect on Threshold Placement	Robustness Interpretation
β	0.25–0.75	Changes the chemical-threshold slope through the exponent $(2+\beta)/3$; high-$\widetilde{\Pi}_S$ threshold positions shift by order tens of percent across the tested range.	Qualitative separation between sulfur-saturated and chemically amplified regimes persists.
m	1–4	Changes the sharpness of the transition near $\widetilde{\Pi}_S \sim 1$ but leaves the low- and high-burden asymptotic scalings unchanged	Onset location is somewhat closure-dependent; asymptotic regime ordering is stable.
$\Gamma_{\min}$	0.02–0.12	Does not move the microphysical or chemical threshold lines; affects the decay tail only when the raw removal rate would fall below the admissibility floor.	Lifetime magnitude in the most confined cases is floor-sensitive; early-to-intermediate regime ordering is unchanged.

Table 12 summarizes the conclusions supported by the local sensitivity tests and distinguishes them from closure-dependent outcomes.

Table 12. Robustness matrix summarizing which conclusions are supported directly by the local sensitivity tests and which remain closure- or range-dependent.

Conclusion	Support Within the Explored Neighborhood	Status
Microphysical saturation reduces forcing efficiency	Follows analytically from the burden–radius scaling and remains visible under moderate perturbations of β, m, and B_c	Structurally robust within the adopted bridge-law family
Chemically amplified ozone loss requires the halogen–surface-area product to exceed threshold	Supported by Equation (20), the regime map, and the sensitivity of X_{pk} to Π_H, δ_O, and β	Locally robust, but quantitatively closure-dependent
Ash reduces integrated optical-depth proxy at fixed nominal loading	Isolated by the ash-only trajectory and by the (Da_A, χ) interaction test	Locally robust for the tested uptake range
Confinement modifies late decay and lifetime diagnostics	Appears in the χ perturbations and in the interaction with $\Gamma_{\min}$	Most sensitive to closure, floor, and integration horizon
Benchmark sectors organize published case classes	Supported by explicit mapping equations, worked ranges, and anchor-case consistency	Interpretive only; not calibrated event retrieval

7. Discussion: Implications for Model Hierarchy and Interpretation

The interpretive statements in this section are intentionally graded. They refer to the response families resolved within the explored parameter neighborhood and chosen integration horizon, not to a global survey of the full control space. Results shown directly by the reduced theory are therefore kept separate from broader hypotheses suggested for chemistry–climate applications.

7.1. Results Shown Directly by the Reduced Theory

Several results are demonstrated directly by the reduced equations and integrations. First, once the generalized radius bridge law enters the strong-burden regime, optical depth and aerosol surface area grow sublinearly with sulfur input while the sedimentation tendency strengthens. Second, chemically amplified ozone loss emerges only when the product of halogen availability and aerosol surface area crosses the $\Lambda \sim 1$ threshold. Third, ash shifts both radiative and chemical thresholds by reducing the sulfur yield available to the sulfate aerosol. Fourth, the sign of the bulk stratospheric thermal anomaly feeds back onto residence time through Equation (23). These are outcomes of the reduced theory itself and do not require any external interpretation.

7.2. Hypotheses Suggested by the Reduced Theory

Other statements should be interpreted more carefully as hypotheses suggested by the reduced theory rather than as results demonstrated by it. The analysis suggests that chemistry–climate model ensembles should not vary sulfur mass alone; they should also sample halogen delivery, ash persistence, and dynamical state. It also suggests that stratospheric transport state can shift the realized response even at fixed source parameters, while the revised formulation keeps lifetime control (χ) separate from hemispheric partitioning (ψ) unless a specific benchmark study justifies coupling them. These implications are consistent with the existing modeling literature, but the reduced model does not by itself resolve jets, the QBO, or three-dimensional transport.

7.3. Broader Inferences Consistent with the Literature

The reduced-order theory is also consistent with broader inferences drawn from published Toba-like and Los Chocoyos-like studies. In particular, it provides a compact explanation for why severe short-lived atmospheric-chemical disruption can coexist with a more limited long-duration cooling signal: forcing efficiency can saturate while aerosol surface area remains large enough to sustain strong heterogeneous chemistry. That inference is consistent with, but not proven by, the reduced theory. The benchmark sectors used in this interpretation remain interpretive, heuristic regime placements rather than calibrated event estimates. More broadly, the model offers a compact language for volcanic hazard, paleoclimate interpretation, and ensemble design, but it should not be mistaken for a replacement for vertically resolved chemistry–climate simulations or coupled Earth-system modeling.

8. Discussion: Limitations and Extensions

Several limitations should be stated explicitly. First, the chemical scheme is reduced to a single effective halogen variable and a single ozone-loss equation. This is sufficient for threshold analysis but not for quantitative prediction of chlorine, bromine, nitrogen, and HO_x partitioning [14,16]. Second, the aerosol population is represented by an effective radius and a burden, with detailed sectional or modal microphysics absorbed into the exponent β or the bridge law in Equation (12). This is analytically efficient but cannot reproduce detailed size distributions or wavelength-dependent optical properties, and it is most likely to break down when broad size spectra or composition- and humidity-dependent optics materially decouple optical-depth and surface-area behavior [2,6,12]. In such cases, quantitative placement of chemical versus radiative thresholds could shift even if the qualitative regime structure remains useful. Third, the lifetime-control parameter χ and the diagnostic asymmetry coordinate ψ are low-dimensional surrogates for a genuinely high-dimensional circulation problem. They expose sensitivity and permit controlled decoupling tests, but they do not predict circulation from first principles [21,22]. Accordingly, the model should not be evaluated through a single numerical error margin against resolved chemistry–climate simulations; its appropriate comparison class is regime topology, sign, and ordering across published model behaviors. Fourth, ocean coupling and carbon-cycle feedback are omitted, so the theory concerns the atmospheric-to-interannual problem rather than full Earth-system recovery [3].

These limitations are not defects of principle; they identify the next level of theory. The reduced-order system could be extended by introducing an explicit vertical coordinate, separate tropical and extratropical boxes, a resolved ash reservoir, a water-vapor perturbation variable, or a prognostic QBO-shear coordinate. A stochastic extension of χ would allow internal variability to be sampled probabilistically. A Bayesian calibration against ensembles of chemistry–climate model output would convert the present deterministic regime map into a quantitatively constrained emulator. Such developments would preserve the analytical clarity of the regime theory while improving fidelity.

9. Conclusions

A reduced-order analysis has been developed for the coupled evolution of stratospheric sulfur, sulfate aerosol burden, reactive halogens, fractional ozone loss, and a bulk stratospheric thermal anomaly after sulfur-rich volcanic eruptions. The aim has been interpretive rather than predictive: to identify the minimum set of control parameters required to organize the nonlinear coupling among sulfur loading, aerosol growth, ash scavenging, ozone loss, and dynamical state.

The principal results are as follows:

1. A sulfur-loading threshold exists because optical depth and aerosol surface area scale as $B^{(2+\beta)/3}$ rather than linearly once particle growth departs from the quasi-linear regime. The forcing efficiency therefore declines as sulfur loading increases beyond the onset of microphysical saturation [4,7,8].
2. A chemically amplified regime emerges when the halogen–surface-area product exceeds the inverse ozone-recovery timescale. Severe ozone loss can therefore coexist with sublinear radiative scaling [15,16,18].
3. Ash scavenging modifies both the radiative and chemical branches by reducing sulfur yield before the sulfate cloud matures, thereby shifting multiple thresholds at once [19].
4. The sign of the bulk thermal response is governed by competition between aerosol heating and ozone-loss cooling; when cooling dominates, self-lofting is suppressed and aerosol residence time shortens [5,16].
5. Expanded local sensitivity tests around representative states indicate that, within the explored parameter neighborhood and chosen integration horizon, the main response families remain identifiable under moderate perturbations of the principal closures, whereas the precise magnitude of peak ozone loss, integrated optical depth, and lifetime remains closure-dependent and becomes most uncertain in strongly confined cases.

These robustness statements are intentionally local rather than global: they apply only to response families resolved within the explored parameter neighborhood and chosen integration horizon, and should not be read as a survey of the full control space; lifetime-related diagnostics in the most confined cases remain partly sensitive to $\Gamma_{\min}$ through the decay tail. The scaling laws, threshold conditions, and sign criteria derived above are direct outcomes of the reduced theory, whereas the benchmark sectors and eruption-class placements are literature-informed, heuristic regime interpretations rather than calibrated event estimates or inverse-retrieved parameters. The shared optical-depth/surface-area closure can also shift quantitative chemical-versus-radiative threshold placement if humidity, composition, or broad size-distribution effects decouple A_s from $\tau_{\mathrm{sw}}(B)$, even though the qualitative regime structure remains useful. The broader implication is that sulfur-rich eruptions are better interpreted as points in a multidimensional regime space than as members of a one-dimensional sequence ordered only by sulfur mass. In that sense, the reduced-order theory is best viewed as a low-dimensional organizing model for experiment design, intercomparison, and interpretation of more comprehensive chemistry–climate simulations.

Supplementary Materials: The following supporting information can be downloaded at: https://www.mdpi.com/article/10.3390/atmos17060606/s1. The Supplementary Materials include the full reproducibility package for this manuscript: the vector figures, the Python scripts used to generate the manuscript figures, the driver script (`run_all_figures.py`), the software-environment files (`requirements.txt` and `environment.yml`), a reproducibility README, the scenario table in CSV form, the benchmark provenance matrix, the anchor-case consistency table, the external-consistency table, the equation-status table, the dynamical-state classification table, the threshold-sensitivity summary, the robustness matrix, the raw-versus-interpretive benchmark table, and the document entitled *Supplementary Benchmark Calculation Sheet* in Portable Document Format (PDF) and comma-separated values (CSV) form. The software-environment files specify the tested environment (Python 3.13.5, NumPy 2.3.5, SciPy 1.17.0, and Matplotlib 3.10.8).

Funding: This research received no external funding.

Institutional Review Board Statement: Not applicable.

Informed Consent Statement: Not applicable.

Data Availability Statement: All data and reproducibility materials supporting this manuscript are provided in the Supplementary Materials.

Acknowledgments: The author thanks the anonymous reviewers for their constructive comments and suggestions, which helped improve the manuscript. OpenAI ChatGPT (GPT-5.5 Pro) was used to assist with LaTeX source preparation, language refinement, and Graphical Abstract drafting. The author reviewed and approved the outputs and assumes full responsibility for the manuscript.

Conflicts of Interest: The author declares no conflict of interest.

Abbreviations

The following abbreviations are used in this manuscript:

ERF	Effective radiative forcing
QBO	Quasi-biennial oscillation
SAOD	Stratospheric aerosol optical depth
SO_2	Sulfur dioxide
H_2SO_4	Sulfuric acid

Appendix A. Derivation of the Burden-Size-Optical-Depth Scaling

Assume $N_c = N_\star (B/B_\star)^\beta$. Then Equation (11) yields

$$r_{\mathrm{eff}} = \left(\frac{3 v_{\mathrm{sulf}} B}{4\pi \rho_p N_\star} \right)^{1/3} \left(\frac{B}{B_\star} \right)^{-\beta/3} \propto B^{(1-\beta)/3}.$$

Substitution into Equation (13) gives

$$\tau_\lambda \propto \frac{B}{B^{(1-\beta)/3}} = B^{1-(1-\beta)/3} = B^{(2+\beta)/3}.$$

The same result holds for A_s because $A_s \propto B/r_{\mathrm{eff}}$. The quasi-linear limit is $\beta = 1$. The coagulation-dominated limit is $\beta = 0$.

Appendix B. Derivation of the Ash-Modified Sulfur Yield

Starting from Equation (1),

$$\frac{1}{S}\frac{\mathrm{d}S}{\mathrm{d}t} = -\frac{1}{\tau_{\mathrm{ox}}} - \frac{Da_A}{\tau_{\mathrm{ox}}} \exp\!\left(-\frac{t}{\tau_{\mathrm{ash}}} \right).$$

Integration from 0 to t gives

$$\ln\left(\frac{S(t)}{S_0}\right) = -\frac{t}{\tau_{\rm ox}} - Da_A \frac{\tau_{\rm ash}}{\tau_{\rm ox}}\left(1 - \exp\left[-\frac{t}{\tau_{\rm ash}}\right]\right),$$

which immediately yields Equation (3). For $t \gg \tau_{\rm ash}$, the permanent multiplicative suppression of the sulfur reservoir is approximately $\exp[-Da_A \tau_{\rm ash}/\tau_{\rm ox}]$.

Appendix C. Derivation of the Sedimentation Scaling

With $v_s \propto r_{\rm eff}^2$ from Equation (36), the sedimentation timescale satisfies

$$\tau_{\rm sed} \sim \frac{H_s}{v_s} \propto r_{\rm eff}^{-2}.$$

Since $r_{\rm eff} \propto B^{(1-\beta)/3}$,

$$\tau_{\rm sed} \propto B^{-2(1-\beta)/3}.$$

Hence any departure from $\beta = 1$ introduces a burden-dependent reduction in aerosol lifetime.

Appendix D. Benchmark-Mapping Details

The benchmark sectors in Table 7 were obtained by combining three ingredients. First, sulfur loading was translated into the effective benchmark coordinate $\widetilde{\Pi}_S$ using Equation (47) and an onset scale $E_{S,c}$ constrained by the 10–40 Tg S transition corridor identified by [7] and the saturation analysis of [8]. In that mapping, $E_{S,c}$ is defined for a reference sulfate-conversion yield $y_{S,\rm ref}$, so the worked benchmark tables effectively assume $y_S/y_{S,\rm ref} \approx 1$ unless a separate conversion-yield correction is justified. Second, a representative ozone-loss fraction $X_{\rm ref}$ from published sulfur–halogen simulations was converted into $\Lambda_{\rm ref} = X_{\rm ref}/(1 - X_{\rm ref})$ and then into Π_H through Equation (48). Third, ash influence was converted to Da_A through Equation (49). The resulting uncertainty boxes are therefore bounded by literature-informed working ranges rather than by a formal inverse calculation. The tabulated ranges are rounded, expert-trimmed interpretive envelopes based on literature constraints and physical plausibility checks; they are not obtained by mechanically propagating all endpoint combinations. Tables A2 and A3 list the concrete inputs and outputs used to construct Figure 5; the same values are also provided in machine-readable form in the supplementary benchmark sheet. Table A1 records the provenance level of the benchmark quantities so that directly constrained inputs, model-mediated estimates, and expert-trimmed interpretive envelopes are not conflated.

Table A1. Benchmark provenance matrix. Confidence labels indicate the role played by the literature in constraining each quantity; they are not formal statistical probabilities.

Quantity	Evidence Basis	Transformation Used in This Manuscript	Confidence Class
Injected sulfur E_S	Published event or experiment-class sulfur estimates and idealized forcing corridors [7,8]	Normalized by $E_{S,c}$ to form the effective loading coordinate	Direct-to-moderate
Onset scale $E_{S,c}$	Transition between quasi-linear and saturating behavior in model studies [7,8]	Treated as an order-of-magnitude threshold rather than a universal constant	Moderate
Ash yield Y_A	Ash-mediated sulfur-removal estimates [19]	Converted to Da_A through Equation (49) and to $\widetilde{\Pi}_S$ through Equation (47)	Moderate

Table A1. *Cont.*

Quantity	**Evidence Basis**	**Transformation Used in This Manuscript**	**Confidence Class**
ozone-loss proxy X_{ref}	Published halogen-rich eruption simulations [15,16,18]	Converted to Λ_{ref} and then to Π_H through Equation (48)	Theory-mediated
Dynamical class χ	Initial-condition, season, and circulation-sensitivity studies [9,22,23]	Assigned as a bounded lifetime-control class rather than estimated as a retrieved physical observable	Interpretive
Asymmetry coordinate ψ	Hemispheric partition diagnostics when available [22]	Mapped through $\psi = \text{arctanh}(\mathcal{A}_H)$	Moderate when diagnostics exist; otherwise interpretive

Table A2. Worked benchmark inputs for sulfur loading and ash suppression. These are the adopted ranges used to construct the uncertainty boxes in Figure 5.

Class	E_S **(Tg S)**	Y_A	$E_{S,c}$ **(Tg S)**	**Output** $\widetilde{\Pi}_S$	**Output** Da_A
Pinatubo-like	6–12	0.95–1.00	15–18	0.32–0.80	0.00–0.08
Transition corridor	12–24	0.95–1.00	18–20	0.60–1.20	0.00–0.08
Toba-like	65–120	0.82–0.97	18–20	3.0–6.0	0.05–0.30
Los Chocoyos-like	85–145	0.55–0.82	17–20	4.0–7.0	0.30–0.90

Table A3. Worked benchmark inputs for chemical and dynamical placement. χ is treated as a lifetime-control class variable, whereas ψ is diagnosed from asymmetry when a partition estimate is available.

Class	X_{ref}	β_{ref}	**Output** Π_H	χ **Band**	$\mathcal{A}_H$ **Range**	**Output** ψ
Pinatubo-like	0.02–0.05	0.45–0.55	0.03–0.10	−0.10–0.10	−0.10–0.10	−0.10–0.10
Transition corridor	0.05–0.15	0.45–0.55	0.08–0.25	−0.10–0.20	−0.20–0.20	−0.20–0.20
Toba-like	0.30–0.55	0.40–0.50	0.20–0.60	0.00–0.50	0.10–0.40	0.10–0.42
Los Chocoyos-like	0.50–0.80	0.40–0.50	0.50–1.60	0.10–0.60	0.20–0.60	0.20–0.69

The benchmark procedure intentionally preserves two layers. Raw endpoint ranges are computed from the working formulas by combining the extreme input values in Tables A2 and A3; interpretive ranges then apply the same rounding and physical-plausibility constraints used in Figure 5. Table A4 reports both layers so that the heuristic trimming is visible rather than hidden.

Table A4. Raw endpoint propagation versus interpretive benchmark envelopes. Raw ranges are obtained directly from the working formulas, whereas interpretive envelopes are rounded and expert-trimmed to preserve consistency with the anchor-case behavior in Table 8.

Class	**Raw** $\widetilde{\Pi}_S$	**Interpretive** $\widetilde{\Pi}_S$	**Raw** Π_H	**Interpretive** Π_H
Pinatubo-like	0.32–0.80	0.32–0.80	0.02–0.14	0.03–0.10
Transition corridor	0.57–1.33	0.60–1.20	0.05–0.27	0.08–0.25
Toba-like	2.67–6.47	3.00–6.00	0.10–0.51	0.20–0.60
Los Chocoyos-like	2.34–6.99	4.00–7.00	0.20–1.32	0.50–1.60

Appendix E. Additional Tables

Tables A5 and A6 provide the expanded symbol list and qualitative regime classification used as reference material for the main text. Additional machine-readable supplementary CSV files provide the equation-status summary, external-consistency check, dynamical-state classification, and threshold-sensitivity summary.

Table A5. Expanded symbol table for the reduced-order theory.

Symbol	Interpretation	Comment
S	Sulfur-equivalent gas-phase burden	Sulfur residing in the stratospheric sulfur dioxide (SO_2) reservoir
B	Sulfur-equivalent sulfate burden	Sulfur carried by sulfate aerosol; aerosol mass is $B_{\mathrm{aer}} = \nu_{\mathrm{sulf}} B$
N_c	Aerosol particle number column	Explicit or implicit microphysical state variable
r_{eff}	Effective particle radius	Diagnostic of the burden–number ratio and sedimentation
H	Effective reactive-halogen burden	Reduced representation of chemically active chlorine and bromine
X	Fractional ozone loss	$X = 1 - \Omega/\Omega_b$
T_s	Stratospheric thermal anomaly	Net effect of aerosol heating and ozone-loss cooling
Π_S	Sulfur-loading parameter	Burden relative to onset of microphysical saturation
Π_H	Halogen parameter	Reactive halogen strength relative to ozone-loss threshold
Da_A	Ash-uptake Damköhler number	Early ash scavenging relative to gas-phase oxidation
χ	Lifetime-control parameter	Encodes confinement/export sensitivity and initial-state dependence in the residence-time branch
ψ	Diagnostic asymmetry coordinate	Encodes partitioning toward the preferred versus opposite hemisphere

Table A6. Qualitative regime classification implied by the revised reduced-order theory.

Regime	Approximate Condition	Dominant Behavior	Representative Literature Context
Quasi-linear sulfur regime	$\Pi_S \ll 1, \beta \approx 1$	Optical depth nearly proportional to sulfur; effective radius weakly varying	Moderate tropical eruptions and the idealized 10–40 Tg S range [7,10]
Microphysical saturation regime	$\Pi_S \gtrsim 1, \beta < 1$	Sublinear forcing growth, faster sedimentation, declining forcing efficiency	Large or super-eruptive sulfur injections [4,5,8]
Chemically amplified regime	$\Lambda \gtrsim 1$ or $\Pi_H \Pi_S^{(2+\beta)/3} \gtrsim 1$	Strong ozone depletion and possible suppression of self-lofting	Halogen-rich Los Chocoyos- and Toba-like scenarios [15,16,18]
Ash-modified regime	Da_A non-negligible	Reduced sulfur yield into sulfate and displaced radiative and chemical thresholds	Persisting ash affecting early SO_2 loss [19]
State-dependent dynamical regime	$\lvert\chi\rvert$ non-negligible and/or $\lvert\psi\rvert$ non-negligible	Residence-time sensitivity and, when diagnosed, hemispheric asymmetry linked to season, QBO, and initial circulation	Initial-condition spread and circulation sensitivity [20,22–24]

References

1. Robock, A. Volcanic eruptions and climate. *Rev. Geophys.* **2000**, *38*, 191–219. [CrossRef]
2. Kremser, S.; Thomason, L.W.; von Hobe, M.; Hermann, M.; Deshler, T.; Timmreck, C.; Toohey, M.; Stenke, A.; Schwarz, J.P.; Weigel, R.; et al. Stratospheric aerosol—Observations, processes, and impact on climate. *Rev. Geophys.* **2016**, *54*, 278–335. [CrossRef]
3. Marshall, L.R.; Maters, E.C.; Schmidt, A.; Timmreck, C.; Robock, A.; Toohey, M. Volcanic effects on climate: Recent advances and future avenues. *Bull. Volcanol.* **2022**, *84*, 54. [CrossRef]
4. English, J.M.; Toon, O.B.; Mills, M.J. Microphysical simulations of large volcanic eruptions: Pinatubo and Toba. *J. Geophys. Res. Atmos.* **2013**, *118*, 1880–1895. [CrossRef]
5. Niemeier, U.; Schmidt, H. Changing transport processes in the stratosphere by radiative heating of sulfate aerosols. *Atmos. Chem. Phys.* **2017**, *17*, 14871–14886. [CrossRef]
6. Wrana, F.; Niemeier, U.; Thomason, L.W.; Wallis, S.; von Savigny, C. Stratospheric aerosol size reduction after volcanic eruptions. *Atmos. Chem. Phys.* **2023**, *23*, 9725–9743. [CrossRef]
7. Timmreck, C.; Olonscheck, D.; Ballinger, A.P.; D'Agostino, R.; Fang, S.W.; Schurer, A.P.; Hegerl, G.C. Linearity of the climate response to increasingly strong tropical volcanic eruptions in a large ensemble framework. *J. Clim.* **2024**, *37*, 2455–2470. [CrossRef]
8. Enger, E.R.; Graversen, R.; Theodorsen, A. Saturation in forcing efficiency and temperature response of large volcanic eruptions. *J. Geophys. Res. Atmos.* **2025**, *130*, e2024JD041098. [CrossRef]
9. Toohey, M.; Krüger, K.; Niemeier, U.; Timmreck, C. The influence of eruption season on the global aerosol evolution and radiative impact of tropical volcanic eruptions. *Atmos. Chem. Phys.* **2011**, *11*, 12351–12367. [CrossRef]
10. Marshall, L.R.; Smith, C.J.; Forster, P.M.; Aubry, T.J.; Andrews, T.; Schmidt, A. Large variations in volcanic aerosol forcing efficiency due to eruption source parameters and rapid adjustments. *Geophys. Res. Lett.* **2020**, *47*, e2020GL090241. [CrossRef]

11. Quaglia, I.; Timmreck, C.; Niemeier, U.; Visioni, D.; Pitari, G.; Brodowsky, C.; Brühl, C.; Dhomse, S.S.; Franke, H.; Laakso, A.; et al. Interactive stratospheric aerosol models' response to different amounts and altitudes of SO_2 injection during the 1991 Pinatubo eruption. *Atmos. Chem. Phys.* **2023**, *23*, 921–948. [CrossRef]
12. Clyne, M.; Lamarque, J.F.; Mills, M.J.; Khodri, M.; Ball, W.; Bekki, S.; Dhomse, S.S.; Lebas, N.; Mann, G.; Marshall, L.; et al. Model physics and chemistry causing intermodel disagreement within the VolMIP-Tambora interactive stratospheric aerosol ensemble. *Atmos. Chem. Phys.* **2021**, *21*, 3317–3343. [CrossRef]
13. Toohey, M.; Jia, Y.; Khanal, S.; Tegtmeier, S. Stratospheric residence time and the lifetime of volcanic stratospheric aerosols. *Atmos. Chem. Phys.* **2025**, *25*, 3821–3839. [CrossRef]
14. Brenna, H.; Kutterolf, S.; Krüger, K. Global ozone depletion and increase of UV radiation caused by pre-industrial tropical volcanic eruptions. *Sci. Rep.* **2019**, *9*, 9435. [CrossRef]
15. Brenna, H.; Kutterolf, S.; Mills, M.J.; Krüger, K. The potential impacts of a sulfur- and halogen-rich supereruption such as Los Chocoyos on the atmosphere and climate. *Atmos. Chem. Phys.* **2020**, *20*, 6521–6539. [CrossRef]
16. Staunton-Sykes, J.; Aubry, T.J.; Shin, Y.M.; Weber, J.; Marshall, L.R.; Abraham, N.L.; Archibald, A.; Schmidt, A. Co-emission of volcanic sulfur and halogens amplifies volcanic effective radiative forcing. *Atmos. Chem. Phys.* **2021**, *21*, 9009–9029. [CrossRef]
17. Osterstrom, F.F.; Klobas, J.E.; Kennedy, R.P.; Cadoux, A.; Wilmouth, D.M. Sensitivity of stratospheric ozone to the latitude, season, and halogen content of a contemporary explosive volcanic eruption. *Sci. Rep.* **2023**, *13*, 6457. [CrossRef]
18. Osipov, S.; Stenchikov, G.; Tsigaridis, K.; LeGrande, A.N.; Bauer, S.E.; Fnais, M.; Lelieveld, J. The Toba supervolcano eruption caused severe tropical stratospheric ozone depletion. *Commun. Earth Environ.* **2021**, *2*, 71. [CrossRef]
19. Zhu, Y.; Toon, O.B.; Jensen, E.J.; Bardeen, C.G.; Mills, M.J.; Tolbert, M.A.; Yu, P.; Woods, S. Persisting volcanic ash particles impact stratospheric SO_2 lifetime and aerosol optical properties. *Nat. Commun.* **2020**, *11*, 4526. [CrossRef] [PubMed]
20. DallaSanta, K.J.; Gerber, E.P.; Toohey, M. The circulation response to volcanic eruptions: The key roles of stratospheric warming and eddy interactions. *J. Clim.* **2019**, *32*, 1101–1120. [CrossRef]
21. Butchart, N. The stratosphere: A review of the dynamics and variability. *Weather Clim. Dyn.* **2022**, *3*, 1237–1272. [CrossRef]
22. Zhuo, Z.; Fuglestvedt, H.F.; Toohey, M.; Krüger, K. Initial atmospheric conditions control transport of volcanic volatiles, forcing and impacts. *Atmos. Chem. Phys.* **2024**, *24*, 6233–6249. [CrossRef]
23. DallaSanta, K.; Orbe, C.; Rind, D.; Nazarenko, L.; Jonas, J. Response of the quasi-biennial oscillation to historical volcanic eruptions. *Geophys. Res. Lett.* **2021**, *48*, e2021GL095412. [CrossRef]
24. Brenna, H.; Kutterolf, S.; Mills, M.J.; Niemeier, U.; Timmreck, C.; Krüger, K. Decadal disruption of the QBO by tropical volcanic supereruptions. *Geophys. Res. Lett.* **2021**, *48*, e2020GL089687. [CrossRef]
25. Black, B.A.; Lamarque, J.-F.; Marsh, D.R.; Schmidt, A.; Bardeen, C.G. Global climate disruption and regional climate shelters after the Toba supereruption. *Proc. Natl. Acad. Sci. USA* **2021**, *118*, e2013046118. [CrossRef]
26. Innes, H.M.; Hutchison, W.; Sigl, M.; Crick, L.; Abbott, P.M.; Bigler, M.; Chellman, N.J.; Davies, S.M.; Kutterolf, S.; McConnell, J.R.; et al. Ice core evidence for the Los Chocoyos supereruption disputes millennial-scale climate impact. *Commun. Earth Environ.* **2025**, *6*, 137. [CrossRef]
27. Aubry, T.J.; Toohey, M.; Marshall, L.R.; Schmidt, A.; Jellinek, A.M. A New Volcanic Stratospheric Sulfate Aerosol Forcing Emulator (EVA_H): Comparison with Interactive Stratospheric Aerosol Models. *J. Geophys. Res. Atmos.* **2020**, *125*, e2019JD031303. [CrossRef]
28. Devine, J.D.; Sigurdsson, H.; Davis, A.N.; Self, S. Estimates of sulfur and chlorine yield to the atmosphere from volcanic eruptions and potential climatic effects. *J. Geophys. Res.* **1984**, *89*, 6309–6325. [CrossRef]
29. Kutterolf, S.; Hansteen, T.H.; Appel, K.; Freundt, A.; Krüger, K.; Pérez, W.; Wehrmann, H. Combined bromine and chlorine release from large explosive volcanic eruptions: A threat to stratospheric ozone? *Geology* **2013**, *41*, 707–710. [CrossRef]
30. Kutterolf, S.; Hansteen, T.H.; Freundt, A.; Wehrmann, H.; Appel, K.; Krüger, K.; Pérez, W. Bromine and chlorine emissions from Plinian eruptions along the Central American Volcanic Arc: From source to atmosphere. *Earth Planet. Sci. Lett.* **2015**, *429*, 234–246. [CrossRef]
31. Vidal, C.M.; Métrich, N.; Komorowski, J.-C.; Pratomo, I.; Michel, A.; Kartadinata, N.; Robert, V.; Lavigne, F. The 1257 Samalas eruption (Lombok, Indonesia): The single greatest stratospheric gas release of the Common Era. *Sci. Rep.* **2016**, *6*, 34868. [CrossRef] [PubMed]
32. Hunter, J.D. Matplotlib: A 2D Graphics Environment. *Comput. Sci. Eng.* **2007**, *9*, 90–95. [CrossRef]
33. Virtanen, P.; Gommers, R.; Oliphant, T.E.; Haberland, M.; Reddy, T.; Cournapeau, D.; Burovski, E.; Peterson, P.; Weckesser, W.; Bright, J.; et al. SciPy 1.0: Fundamental Algorithms for Scientific Computing in Python. *Nat. Methods* **2020**, *17*, 261–272. [CrossRef]
34. Harris, C.R.; Millman, K.J.; van der Walt, S.J.; Gommers, R.; Virtanen, P.; Cournapeau, D.; Wieser, E.; Taylor, J.; Berg, S.; Smith, N.J.; et al. Array programming with NumPy. *Nature* **2020**, *585*, 357–362. [CrossRef] [PubMed]